

The blue supergiant Sher 25 revisited in the Gaia era

D. Weißmayer¹, N. Przybilla¹, A. Ebenbichler¹, P. Aschenbrenner¹, and K. Butler²

¹ Universität Innsbruck, Institut für Astro- und Teilchenphysik, Technikerstr. 25/8, 6020 Innsbruck, Austria
e-mail: david.wessmayer@uibk.ac.at ; norbert.przybilla@uibk.ac.at

² Ludwig-Maximilians-Universität München, Universitätssternwarte, Scheinerstr. 1, 81679 München, Germany

Received ; accepted

ABSTRACT

Aims. The evolutionary status of the blue supergiant Sher 25 and its membership to the massive cluster NGC 3603 are investigated. **Methods.** A hybrid non-LTE (local thermodynamic equilibrium) spectrum synthesis approach is employed to analyse a high-resolution optical spectrum of Sher 25 and five similar early B-type comparison stars in order to derive atmospheric parameters and elemental abundances. Fundamental stellar parameters are determined by considering stellar evolution tracks, Gaia Data Release 3 (DR3) data and complementary distance information. Interstellar reddening and the reddening law along the sight line towards Sher 25 are constrained employing UV photometry for the first time in addition to optical and infrared data. The distance to NGC 3603 is reevaluated based on Gaia DR3 data of the innermost cluster O-stars.

Results. The spectroscopic distance derived from the quantitative analysis implies that Sher 25 lies in the foreground of NGC 3603, which is found to have a distance of $d_{\text{NGC3603}} = 6250 \pm 150$ pc. A cluster membership is also excluded as the hourglass nebula is unaffected by the vigorous stellar winds of the cluster stars and from the different excitation signatures of the hourglass nebula and the nebula around NGC 3603. Sher 25 turns out to have a luminosity of $\log L/L_{\odot} = 5.48 \pm 0.14$, equivalent to that of a $\sim 27 M_{\odot}$ supergiant in a single-star scenario, which is about half of the mass assumed so far, bringing it much closer in its characteristics to Sk-69°202, the progenitor of SN 1987A. Sher 25 is significantly older than NGC 3603. Further arguments for a binary (merger) evolutionary scenario of Sher 25 are discussed.

Key words. Stars: abundances – Stars: atmospheres – Stars: early-type – Stars: evolution – Stars: fundamental parameters – supergiants

1. Introduction

The star Sher 25 (Sher 1965) is an intriguing blue supergiant (BSG) close to the massive Galactic cluster NGC 3603. It is located at about 20'' distance north of the cluster centre, see Fig. 1 for a composite image of the field, combining optical and near infrared observations with the Hubble Space Telescope (HST) with near-infrared observations obtained within the Two Micron All Sky Survey (2MASS). The sight line is complex and crowded, aligned over a long stretch of the Carina-Sagittarius spiral arm and characterised by varying reddening towards individual stars and variable nebular emission throughout the field (Pang et al. 2011). Sher 25 shows a surrounding hourglass-shaped nebula (Brandner et al. 1997b;a), similar to the triple ring nebula expelled by the precursor of SN 1987A (Wampler et al. 1990; Burrows et al. 1995). This nebula, in combination with the spectral similarity of Sher 25 (classified as B1 Iab, Melena et al. 2008) to the SN 1987A progenitor star Sk-69°202 (classified as B0.7-3 I, Walborn et al. 1989), raised the prospect of studying a near-twin to a core-collapse supernova progenitor with modern observational data and analysis tools.

Smartt et al. (2002) reported the first model atmosphere analysis of Sher 25. They employed the TLUSTY code (Hubeny 1988), where deviations from the assumption of local thermodynamic equilibrium (LTE) – so-called non-LTE effects – were allowed for in the atmospheric structure computation, but metal-blanketing effects were neglected. On the basis of the model atmospheres, non-LTE line-formation calculations with earlier versions of the codes as used here (see Sect. 3) were conducted.

Sher 25 was found to be highly luminous (adopting a distance to NGC 3603 of 6.3 kpc), with $\log L/L_{\odot} = 5.9 \pm 0.2$, implying a zero-age main sequence (ZAMS) mass of around $60 M_{\odot}$. The surface CNO abundances were found to show some mixing with nuclear-processed material but to be incompatible with a previous red supergiant (RSG) phase of Sher 25 where highly-efficient convective dredge-up would have occurred, such that the nebula was likely ejected during the BSG phase. The overall picture put Sher 25 closer in nature to the high-mass Luminous Blue Variables (LBVs) than to the precursor of SN 1987A. Some LBVs produce ring nebulae as found around the candidate LBVs HD 168625 (Smith 2007) and [SBW2007] 1 (Smith et al. 2007), see also Weis (2011).

The reanalysis of Sher 25 with metal line-blanketed hydrostatic (TLUSTY) and unified (photosphere+wind) non-LTE model atmospheres (FASTWIND, Puls et al. 2005; CMFGEN, Hillier & Miller 1998) by Hendry et al. (2008) confirmed the earlier findings. Using a refined distance to NGC 3603 of 7.6 kpc and a consistent line-of-sight extinction (Melena et al. 2008) a luminosity of $\log L/L_{\odot} = 5.78$ was adopted, indicating a ZAMS mass of $50 \pm 10 M_{\odot}$. In addition, the quantitative analysis of the surrounding nebula by Hendry et al. (2008) confirmed its highly nitrogen-rich composition, while the oxygen abundance resembled that of the NGC 3603 background nebula. Radial velocity variations reported by Hendry et al. (2008) were later suggested to be due to pulsations of Sher 25 and not due to binarity (Taylor et al. 2014).

With regard to the origin of hourglass or ring nebulae, a binary merger scenario is likely for the precursor of SN 1987A

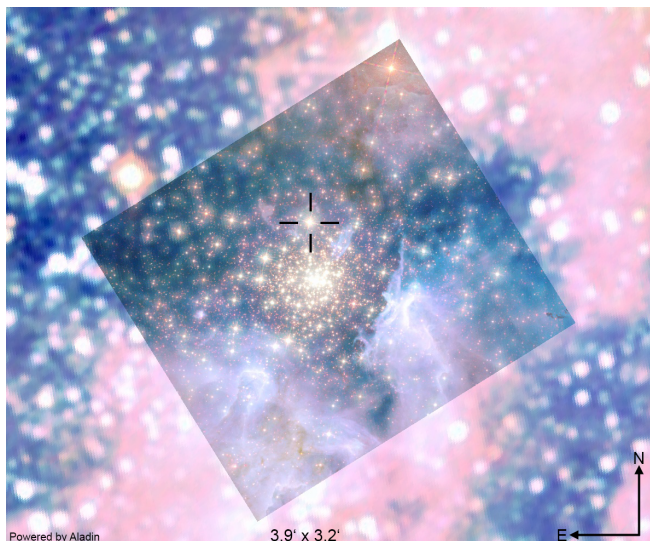


Fig. 1. Colour composite of the field of NGC 3603, with Sher 25 marked by the crosshairs. The centre shows a semi-transparent Hubble Space Telescope Wide Field Camera 3 (HST/WFC3) image (proposal ID: 11360, PI: Robert O’Connell) with the following colour coding: blue (F656N filter), green (F673N), yellow (F128N) and red (F164N). The background shows a 2MASS colour image composed of J ($1.235\ \mu\text{m}$, blue), H ($1.662\ \mu\text{m}$, green) and K_s exposures ($2.159\ \mu\text{m}$, red).

(Podsiadlowski 1992; Morris & Podsiadlowski 2007), with the nebula shaped by the interaction of the common-envelope ejecta with the fast stellar wind of the BSG resulting from the merger. Alternatively, a single-star scenario for ring nebula production may also be at work (Chita et al. 2008), where the fast anisotropic stellar wind of a BSG on a blue loop catches up with the slow spherical wind expelled during a previous RSG phase. Both scenarios require that the star which ejected the nebula had reached the RSG stage earlier in its life, whereas high-mass LBVs eject nebulae as BSGs (Lamers et al. 2001).

The parent cluster of Sher 25, NGC 3603, also deserves a few remarks. Located in the Carina-Sagittarius spiral arm, it is the densest concentration of massive stars known in the Milky Way. It contains several dozen early O-type stars and four WN6h stars (including two in one of the most massive binaries of the Milky Way) that power the surrounding giant H II region. The starburst cluster has an age of 1 ± 1 Myr (Sung & Bessell 2004a; Melena et al. 2008) and shows ongoing star formation in the surrounding nebular knots. There are also indications for subsequent star formation, as Sher 25 and a second BSG, Sher 23, are about 3 Myr older than the stars at the cluster centre (Melena et al. 2008).

However, when taking a closer look, one finds contradictions in the overall picture. If Sher 25 is indeed a member of NGC 3603, why is the hourglass nebula unaffected by the stellar winds from the cluster members that have otherwise cleared the sight line towards the cluster and have shaped cold molecular pillars at even larger lateral distances from the cluster centre, see Fig. 1? Why does the hourglass nebula show a low-excitation emission spectrum despite supposedly being in the presence of one of the most intense UV environments known in the Milky Way, while the spectrum of the surrounding H II region shows the expected high excitation? Why is Sher 25 located close to the evolutionary track of a $\sim 30 M_{\odot}$ ZAMS star in a Kiel diagram (surface gravity vs. effective temperature), whereas it is close to a $\sim 50 M_{\odot}$ track in the Hertzsprung-Russell diagram (HRD)?

The answer may lie in the complex line-of-sight towards NGC 3603, which traverses the Carina-Sagittarius arm over a

range of many kpc. A location of Sher 25 in the fore- or background of the cluster could solve the contradictions and, even more, it would also remove the necessity for subsequent star formation having occurred in NGC 3603. We therefore employ data from the Gaia Data Release 3 (DR3, Gaia Collaboration et al. 2016; Gaia Collaboration 2022) to re-investigate the cluster membership of Sher 25, and our recently introduced hybrid non-LTE spectral analysis methodology (Weßmayer et al. 2022, henceforth Paper I) to readdress its evolutionary status.

The paper is organised as follows: the observational material on Sher 25 and the comparison stars is summarised in Sect. 2 and Sect. 3 concentrates on the models and the analysis methodology. The analysis results are presented in Sect. 4, a summary of the individual comparison stars is given in Sect. 5 and a discussion of Sher 25 in Sect. 6. An IR excess along the sight line to the cluster NGC 3603 is discussed in Appendix A, a Gaia-based distance to NGC 3603 is derived in Appendix B and the model fit to the observed spectrum of Sher 25 is visualised in Appendix C.

2. Observational data

As the spectral type B1 of Sher 25 lies slightly outside the range covered in Paper I, an additional five supergiants of types B1.5 to B0.7 were selected for comparison here. The quantitative analyses of high-quality spectra of B-type supergiants will thus be extended to hotter effective temperatures, based on the same homogeneous analysis methodology.

Phase 3 data on three individual spectra of Sher 25, and data for HD 114199 and HD 152235, as observed with the Fiberfed Extended Range Optical Spectrograph (FEROS, Kaufer et al. 1999) on the Max-Planck-Gesellschaft/European Southern Observatory (ESO) 2.2 m telescope at La Silla in Chile were downloaded from the ESO Science Portal¹. They cover a useful wavelength range from about 3800 to 9200 Å at $R = \lambda/\Delta\lambda \approx 48\,000$. The Sher 25 spectra, which were taken in one night, were co-added in order to increase the S/N . A pipeline-reduced spectrum of HD 91316 (ρ Leo) as observed with the Echelle Spectro-Polarimetric Device for the Observation of Stars (ESPADOnS, Manset & Donati 2003) on the 3.6 m Canada-France-Hawaii telescope (CFHT) at Mauna Kea/Hawaii was downloaded from the CFHT Science Archive at the Canadian Astronomy Data Centre². It covers a wavelength range from about 3700 to 10 500 Å at a resolving power of $R = \lambda/\Delta\lambda \approx 68\,000$. The FEROS and ESPADOnS spectra were normalised by fitting a spline function through carefully selected continuum points.

Finally, HD 13854 and HD 14956 were observed with the Fibre Optics Cassegrain Echelle Spectrograph (FOCES, Pfeiffer et al. 1998) on the 2.2 m telescope at the Calar Alto Observatory in Spain. The FOCES spectra cover a wavelength range from 3860 to 9400 Å with $R \approx 40\,000$. For FOCES the raw data needed to be reduced. Initially, a median filter was applied to the raw images to remove bad pixels and cosmics. The FOCES semi-automatic pipeline (Pfeiffer et al. 1998) was then used for the data reduction: subtraction of bias and darks, flatfielding, wavelength calibration based on Th-Ar exposures, rectification and merging of the echelle orders. In a last step, all spectra were shifted into the laboratory rest frame via cross-correlation with appropriate synthetic spectra.

Figure 2 displays the spectra of the sample stars in three exemplary diagnostic wavelength windows, i) around H δ with Si II and Si IV lines, and several He I and O II lines, ii) the window

¹ <https://archive.eso.org/scienceportal/home>

² <https://www.cadc-ccda.hia-ihp.nrc-cnrc.gc.ca/en/cfht>

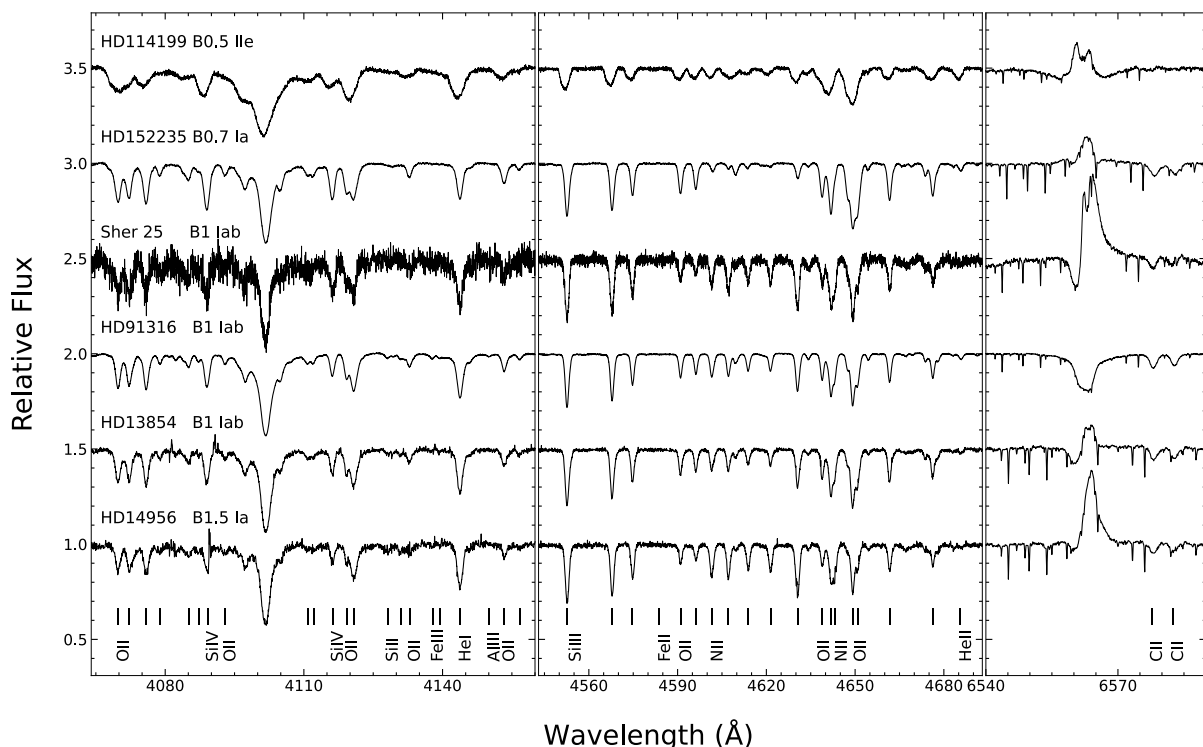


Fig. 2. Sample spectra ordered with respect to spectral type. The panels show spectral windows with prominent features in early B-type supergiants.

Table 1. B-type supergiant sample.

ID #	Object	Sp. T.	OB Assoc./ Cluster	V^a mag	$B - V^a$ mag	Instrument	Date of Obs. YYYY-MM-DD	T_{exp} s	S/N	IUE	
										SW	LW
1	Sher 25	B1 Iab ^b	NGC 3603 ^c	12.275±0.005	1.369±0.010	FEROS	2009-03-22	3×2400	160
2	HD 13854	B1 Iab ^d	Per OB1	6.473±0.017	0.281±0.003	FOCES	2005-09-25	1800	260	P34867	P14595
3	HD 14956	B1.5 Ia ^e	Per OB1	7.204±0.017	0.726±0.014	FOCES	2005-09-25	2800	250	P40231	P19317
4	HD 91316	B1 Iab ^d	Field	3.847±0.014	-0.142±0.007	ESPaDOnS	2008-12-05	2×320	920	P19501	R15529
5	HD 114199	B0.5 IIf ^f	Field	9.474±0.008	0.296±0.011	FEROS	2013-05-08	2×1800	265
6	HD 152235	B0.7 Ia ^d	NGC 6231	6.329±0.021	0.510±0.016	FEROS	2005-04-24	500 + 600	440	P16205	R12470

Notes. ^(a) Mermilliod (1997) ^(b) Melena et al. (2008) ^(c) revised here to: in the foreground of NGC 3603 ^(d) Walborn’s B-type standards (Gray & Corbally 2009) ^(e) Lennon et al. (1992) ^(f) revised here from B1 Ia (Houk et al. 1976)

around the Si III triplet to the He II $\lambda 4686 \text{ \AA}$ line and III) on the $H\alpha$ emission line, with the neighbouring red C II doublet. The narrow features around $H\alpha$ are telluric H_2O lines.

Table 1 summarises important observational information on the sample stars and provides an observing log. An internal ID number is given, the Henry-Draper catalogue designation, the spectral type and an OB association or open cluster membership is indicated. Then, Johnson V magnitudes and the $B - V$ colours are given and the observing log contains information on the spectrograph, the observational date, exposure times, and the resulting S/N of the final spectrum, measured around 5585 \AA .

The star HD 114199, which is subject to a model atmosphere analysis for the first time, was classified as B1 Ia in the literature (Houk et al. 1976). However, closer inspection of the spectrum finds significantly higher rotational velocity than in the other sample stars, broader Balmer lines and ‘double-horned’ emission in $H\alpha$ (see Fig. 2). This is reminiscent of a Be star with an indistinct disk, seen under an intermediate inclination angle, instead of the emission arising from a stellar wind. By comparison with HD 218376 (Cas 1, B0.5 III) from the list of Walborn’s B-type standard stars (Gray & Corbally 2009) HD 114199 is re-

classified as B0.5 IIf here, because of its narrower Balmer lines and an otherwise very similar spectrum.

Several sources of (spectro-)photometric data were employed for the present work in addition to the Echelle spectra. Low-dispersion, large-aperture spectra taken with the International Ultraviolet Explorer (IUE, see also Table 1) were downloaded from the Mikulski Archive for Space Telescopes (MAST³). Photometric measurements in the ultraviolet wavelength range include data from the Astronomical Netherlands Satellite (ANS, Wesselius et al. 1982) and the Belgian/UK Ultraviolet Sky Survey Telescope (S2/68, Thompson et al. 1995) on board the European Space Research Organisation (ESRO) TD1 satellite. For Sher 25, we adopted UV-photometry obtained with the Ultraviolet/Optical Telescope (UVOT) on board the Neil Gehrels Swift Observatory (Yershov 2014). Optical low-resolution spectra were provided by Gaia DR3. In addition, Johnson UBV magnitudes (Mermilliod 1997), $UBVRI$ magnitudes (Sung & Bessell 2004b), JHK magnitudes from the Two Micron All Sky Survey (2MASS, Cutri et al. 2003) and from Harayama et al. (2008), and Wide-Field Infrared Survey Ex-

³ <https://archive.stsci.edu/iue/>

Table 2. Model atoms for non-LTE calculations with DETAIL.

Ion	Terms	Transitions	Reference
H	25	300	[1]
He I/II	29+6/20	162/190	[2]
C II/III	68/70	425/373	[3]
N II	77	462	[4]
O I/II/III	51/176+2/132+2	243/2559/1515	[5]
Ne I/II	153/78	952/992	[6]
Mg II	37	236	[7]
Al III	46+1	272	[8]
Si II/III/IV	52+3/68+4/33+2	357/572/242	[9]
S II/III	78/21	302/34	[10]
Fe III/IV	60+46/65+70	2446/2094	[11]

Notes. Data for different ionisation stages are separated by a slash. If present, the number of superlevels is indicated after a plus sign.

References. [1] Przybilla & Butler (2004); [2] Przybilla (2005); [3] Nieva & Przybilla (2006; 2008); [4] Przybilla & Butler (2001); [5] Przybilla et al. (2000), Przybilla & Butler (in prep.); [6] Morel & Butler (2008); [7] Przybilla et al. (2001); [8] Przybilla (in prep.); [9] Przybilla & Butler (in prep.); [10] Vrancken et al. (1996), updated; [11] Morel et al. (2006), updated.

pler (WISE) photometry (Cutri et al. 2021) were adopted in the course of this work.

3. Models and analysis methodology

The quantitative analysis of B-type supergiants requires consideration of deviations from local thermodynamic equilibrium (non-LTE effects). The hybrid non-LTE approach discussed in Paper I as well as the same analysis technique were adopted for the present work, similar to other applications on e.g. B-type supergiants (Przybilla et al. 2006; Schiller & Przybilla 2008; Farnstein & Przybilla 2012) or on the supergiants' progenitors, early B-type (Nieva & Przybilla 2007; 2012; 2014) and late O-type main-sequence stars (Aschenbrenner et al. 2023), or envelope-stripped massive B-type stars (Irrgang et al. 2022).

In brief, line-blanketed LTE model atmospheres were computed with ATLAS9 (Kurucz 1993), while non-LTE line-formation calculations were performed using extended and updated versions of DETAIL and SURFACE (Giddings 1981; Butler & Giddings 1985), adopting state-of-the-art model atoms. Information on the model atoms is summarised in Table 2, which lists the number of (usually LS -coupled) terms (and superlevels) considered for the given ionisation stage and the number of radiative bound-bound transitions explicitly accounted for in the non-LTE calculations and references where a detailed description of the model atom can be found. The model grids described in Paper I were extended to an effective temperature of 27 000 K. In order to compare the synthetic and observed spectra, the Spectral Plotting and Analysis Suite (SPAS, Hirsch 2009) was used.

The atmospheric parameters were derived using multiple independent spectroscopic indicators simultaneously. The effective temperature T_{eff} and surface gravity $\log g$ were derived by fitting the Stark-broadened Balmer lines and ionisation equilibria of He I/II and several metals, e.g. Si II/III/IV. The microturbulent velocity ξ was determined in the standard way by demanding abundances to be independent of line equivalent widths. Projected rotational velocities $v \sin i$, macroturbulent velocities ζ and the elemental abundances for species X relative to the hydrogen abundance, $\varepsilon(X) = \log(X/H) + 12$, were determined from fits to individual line profiles. The helium abundance y (by number) was derived by considering only the weakest helium lines,

as the saturation of the stronger features restricts their sensitivity to abundance changes.

In order to characterise interstellar reddening, both the total-to-selective extinction $R_V = A_V/E(B - V)$ and the colour excess $E(B - V)$ were determined, with A_V being the interstellar extinction. ATLAS models of the spectral energy distribution (SED) were reddened using the mean extinction law of Fitzpatrick (1999) in order to match the observations. An additional black-body emitter was considered in the case of Sher 25 (see Sect. 6 and Appendix A).

Geneva evolutionary models for rotating stars (Ekström et al. 2012) were used to derive evolutionary masses M_{evol} , which together with the surface gravity values allowed spectroscopic distances d_{spec} to the stars to be derived (see Eq. 3 of Weßmayer et al. 2022). Bolometric corrections $B.C.$ were computed from the ATLAS fluxes. Absolute visual magnitudes M_V were then derived from the apparent V magnitudes and d_{spec} -values, allowing for a determination of M_{bol} and the stellar luminosities L . Stellar radii R were then constrained by combining the luminosities with T_{eff} -values. A comparison with isochrones (from the evolutionary models) provided the evolutionary stellar ages τ_{evol} . Finally, consideration of Gaia DR3 parallaxes provided Gaia-based distances d_{Gaia} , adopted as 'photogeometric distances' of Bailer-Jones et al. (2021).

4. Results

4.1. Atmospheric and fundamental stellar parameters

We summarise the results of the analysis of the sample objects in Table 3, listing the parameters as follows: internal identification number, object name or HD-designation, effective temperature, surface gravity, surface helium abundance (by number), microturbulent, projected rotational and macroturbulent velocities, total-to-selective extinction parameter, colour excess, bolometric correction, absolute visual and bolometric magnitudes, evolutionary mass, radius, luminosity, evolutionary age, spectroscopic and Gaia DR3 distances, that is 'photogeometric' distance estimations (Bailer-Jones et al. 2021). The associated 1σ uncertainty intervals are listed in the line below the derived quantities.

The uncertainties of the derived atmospheric parameters are largely consistent with those reported in Paper I. Effective temperatures were determined with a typical relative accuracy of $\delta T_{\text{eff}} \approx 1\text{--}3\%$ and surface gravities with $\Delta \log g \approx 0.05$ dex. For surface helium abundances, the uncertainties are larger on average, but are generally consistent with $\delta y \approx 10\%$.

The microturbulent velocity parameter is limited in uncertainty to the size and steps of the grid used in the fitting process. Though our analysis considered variations on scales of 1 km s^{-1} in some cases, the general grid was set up with a step size of 2 km s^{-1} , such that we adopt $\Delta \xi \approx 2 \text{ km s}^{-1}$ as a conservative uncertainty margin. Convergence of ATLAS atmospheres permit microturbulence values to reach up to $\xi \leq 17 \text{ km s}^{-1}$ in a few cases, though a value of $\xi = 16 \text{ km s}^{-1}$ may be regarded as an upper limit within our analysis. We wish to stress that sample stars corresponding to this value nevertheless show consistent results across the range of inspected lines, irrespective of strength, species and ionisation stage (see the discussion in Sect. 4.3). The relative uncertainty of the projected rotational velocity amounts to $\delta v \sin(i) \approx 5\text{--}15\%$, while absolute uncertainties for the macroturbulence were generally estimated at a value of 5 km s^{-1} (due to its large rotational velocity and the resulting ambiguity, HD 114199 was assigned an absolute uncertainty in macroturbulence of $\Delta \zeta = 10 \text{ km s}^{-1}$). Uncertainties in total-to-

Table 3. Stellar parameters of the sample stars.

ID#	Object	T_{eff} kK	$\log g$ (cgs)	y	ξ km s ⁻¹	$v \sin i$ km s ⁻¹	ζ	R_V	$E(B - V)$ mag	$B.C.$ mag	M_V mag	M_{bol} mag	M_{evol} M_{\odot}	R R_{\odot}	$\log L/L_{\odot}$	$\log \tau_{\text{evol}}$ yr	d_{spec} pc	d_{Gaia}^a pc
1	Sher 25	20.9	2.61	0.117	16	60	35	3.40	1.66	-1.920	-7.05	-8.97	25.5	42	5.48	6.86	5440	5740
		± 0.5	0.06	0.015	2	5	5	0.1	0.03		0.34	0.34	1.7	7	0.14	0.04	700	⁸⁰⁰ ₄₂₀
2	HD 13854	20.5	2.62	0.111	15	57	47	3.02	0.52	-1.871	-6.91	-8.78	23.7	40	5.41	6.88	2320	2140
		± 0.3	0.04	0.010	2	6	5	0.1	0.03		0.21	0.22	1.0	4	0.09	0.03	200	¹¹⁰ ₁₀₀
3	HD 14956	19.2	2.37	0.127	16	49	55	2.69	0.97	-1.722	-7.55	-9.27	27.2	57	5.60	6.81	2680	2720
		± 0.3	0.04	0.010	2	7	5	0.1	0.03		0.24	0.24	1.5	7	0.10	0.03	250	¹⁵⁰ ₁₃₀
4	HD 91316	21.7	2.87	0.092	15	43	62	2.81	0.09	-2.007	-6.19	-8.20	19.9	28	5.18	6.96	900	660
		± 0.2	0.04	0.009	2	5	5	0.1	0.03		0.20	0.20	1.0	3	0.08	0.04	70	¹⁷⁰ ₁₄₀
4a ^{b,c}											-5.51	-7.52	10.6	20	4.90	
		\pm									0.52	0.53	5.3	5	0.21	
5	HD 114199	25.6	3.42	0.119	14	135	50	3.21	0.59	-2.436	-4.86	-7.29	15.7	13	4.81	7.03	3070	2630
		± 0.4	0.05	0.010	2	9	10	0.1	0.03		0.27	0.27	2.0	2	0.11	0.05	340	¹⁰⁰ ₁₀₀
6	HD 152235	21.6	2.68	0.085	16	59	50	3.00	0.80	-2.006	-6.89	-8.89	24.5	38	5.45	6.87	1460	1620
		± 0.3	0.05	0.008	2	4	5	0.1	0.03		0.24	0.25	1.3	4	0.10	0.04	140	¹³⁰ ₉₀

Notes. Uncertainties are 1σ -values, except where noted otherwise. ^(a) Gaia Collaboration et al. (2016; 2021) – distances and uncertainties correspond to ‘photogeometric distances’ and associated 14th and 86th confidence percentiles (Bailer-Jones et al. 2021). ^(b) Alternative solution, adopting the Gaia distance for the calculation of the fundamental stellar parameters instead of the spectroscopic distance, starting from M_V . ^(c) HD 91316 is in fact a binary star with the V magnitude difference of the two components in the range ~ 1 to 1.5 mag at similar T_{eff} as discussed in Sect. 5. As the Gaia parallax is likely affected by the binary orbital motion (indicated by a high Renormalised Unit Weight Error of 2.457) and in the absence of a second line system, a further determination of the parameters of the binary components is beyond the scope of the present paper.

selective extinction R_V and colour excess $E(B - V)$ depend on the wealth of constraining (spectro-)photometric data available for fitting. However, consistent error-margins of $\Delta R_V = 0.1$ and $\Delta E(B - V) = 0.03$ mag are used to reflect the typical scatter. For the absolute visual and absolute bolometric magnitudes the uncertainties span a range of $\Delta M_V \approx \Delta M_{\text{bol}} = 0.20$ – 0.34 mag.

To determine the evolutionary mass M_{evol} , the sample objects’ location on the spectroscopic Hertzsprung-Russell diagram (sHRD, see the upper panel of Fig. 8) were compared to a grid of evolution tracks by Ekström et al. (2012). Interpolation yielded the ZAMS mass M_{ZAMS} facilitating the derivation of the evolutionary mass by tracing mass loss along the model track. This procedure normally produces uncertainties of $\delta M_{\text{ZAMS}} = \delta M_{\text{evol}} \approx 5\%$, except for stars very close to the end of the main-sequence, specifically HD 114199. As the location of this star is consistent with different evolutionary stages in multiple tracks, its relative uncertainty in M_{evol} and all derived parameters are correspondingly larger than the ‘typical’ values. Stellar radii are determined to typically within $\delta R \approx 10$ – 17% and luminosities to $\Delta \log L/L_{\odot} \approx 0.08$ – 0.14 dex. For the evolutionary age $\log \tau_{\text{evol}}$ of the sample stars, uncertainties are about $\Delta \log \tau_{\text{evol}} \approx 0.04$ dex. The derived spectroscopic distances commonly show relative uncertainties of $\delta d_{\text{spec}} \approx 8$ – 13% , in accordance with the mean relative difference between the deduced values and those inferred from Gaia parallaxes.

4.2. Comparison with previous analyses

Except for HD 114199, every object in the current sample has been analysed in one or even several previous studies. To improve the comparison across the entire B-type supergiant regime, we also include the cooler supergiants of Paper I. For the sake of brevity we refer to our previous work for a description of the methodologies of some of the comparison studies (i.e. Fraser et al. 2010, 7 objects in common; Simón-Díaz et al. 2017, 11 objects; Markova & Puls 2008, 2 objects; Searle et al. 2008, 4 objects). Here, we summarise the additional studies:

i) Crowther et al. (2006) employed the non-LTE stellar atmosphere codes TLUSTY (Hubeny 1988; Hubeny & Lanz 1995) and

CMFGEN (Hillier & Miller 1998) for their analyses. They estimated the effective temperature by matching the intensities of silicon lines of consecutive ionisation stages. For B0–B2 stars as investigated here the silicon line Si iv 4089 Å was compared to the Si iii 4552–4574 multiplet. The surface gravity was constrained by reproducing H γ . For microturbulence, a standard $\xi = 20$ km s⁻¹ was assumed initially and adapted to values in the range of 10–40 km s⁻¹ if the He and Si lines could not be fitted consistently. A uniform abundance ratio of He/H = 0.2 by number was assumed throughout. We have five objects in common. ii) Smartt et al. (2002) used TLUSTY to generate non-LTE, hydrostatic H+He model atmospheres. The effective temperature was determined by fitting the Si iv 4116 Å line and the triplet at Si iii 4813–4830 Å. An estimate of the surface gravity was established by a fit to H γ and H δ . The microturbulent velocity was found by demanding equal abundances of the silicon multiplet Si iii 4552–4574 Å. The projected rotational velocities were determined by convolving model line profiles of multiple metal lines with a rotational broadening function and comparing with observation until a match was produced. Three objects are in common. iii) Hendry et al. (2008) re-analysed the spectra of Sher 25 described above (Smartt et al. 2002), using more advanced stellar atmosphere codes for their re-examination. The following three codes were employed: a refined version of TLUSTY considering metal-line blanketing, the hydrodynamic line-blanketed non-LTE code FASTWIND (Santolaya-Rey et al. 1997; Puls et al. 2005) and CMFGEN. One object (Sher 25) is common.

Figure 3, panel a, shows a comparison of this work’s effective temperatures T_{eff} with those derived in the literature $T_{\text{eff}}^{\text{lit}}$. Large-scale, systematic offsets are absent across the set of discussed studies. When we look at the regime of the earlier supergiants investigated here, a small systematic offset towards higher temperatures may be noticed for some of the literature sets: for Smartt et al. (2002) and Crowther et al. (2006) the relative discrepancy is of the order of 8% and 5%, respectively. The Hendry et al. (2008) analysis shows discrepancies of 0–5%, while the two hottest objects in common with the Simón-Díaz et al. (2017) set are 9% higher in temperature. A significant trend of this sort can be detected neither for the Fraser et al. (2010) nor for the

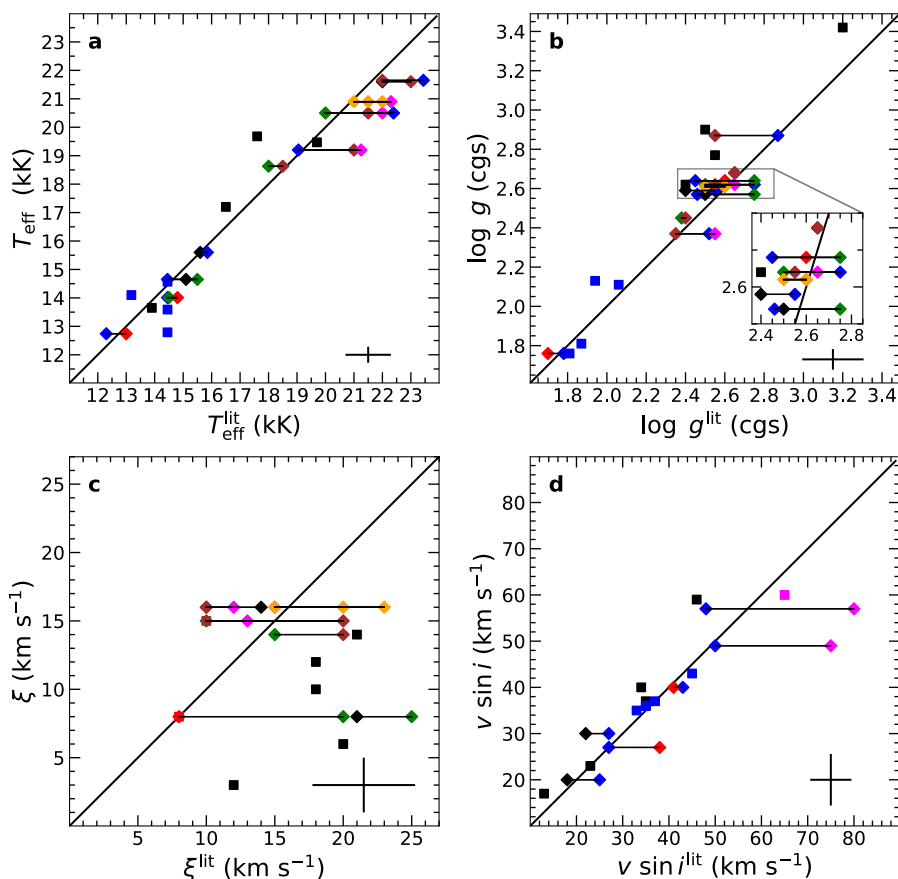


Fig. 3. Comparison of values for effective temperature T_{eff} (panel a), surface gravity $\log g$ (panel b), microturbulence ξ (panel c), and projected rotational velocity $v \sin i$ (panel d) as derived in the present work and Paper I with previous studies: Fraser et al. (2010, black symbols), Simón-Díaz et al. (2017, blue), Markova & Puls (2008, red), Searle et al. (2008, green), Crowther et al. (2006, brown), Smartt et al. (2002, magenta), and Hendry et al. (2008, orange). In cases in which an object is present in two or more studies the values are depicted by diamonds and connected with solid black lines. For better visibility, an inset is added in panel b. Mean error bars of the respective samples are indicated.

Searle et al. (2008) studies. Naturally, these offsets must be put into perspective with the large scatter present between the compared works (i.e. between objects present in two or more literature studies, depicted as connected diamonds in Fig. 3). In the case of HD 13854, the values range from $T_{\text{eff}} = 20$ kK (Searle et al. 2008), to 21.5 kK (Crowther et al. 2006), 22 kK (Smartt et al. 2002) and 22.4 kK (Simón-Díaz et al. 2017). Similarly large ranges exist for all other compared objects.

Values for the surface gravity are compared in Fig. 3, panel b. In Paper I we discussed an emerging trend towards larger values of surface gravity derived using our methodology – here, it is apparent that this effect is significantly diminished by addition of the earlier supergiants of this sample and the inclusion of further studies. However, a general offset persists for the set in common with Fraser et al. (2010), which shows lower surface gravities with $\Delta \log g \approx 0.2$ dex on average. Again, scatter among the studies is high: in the case of HD 13854, the estimates vary from $\log g = 2.5$ (Searle et al. 2008), to 2.55 (Crowther et al. 2006), 2.65 (Smartt et al. 2002) and 2.75 (Simón-Díaz et al. 2017). At maximum, the differences amount to $\Delta \log g \approx 0.3$ dex.

Values for microturbulent velocity ξ are shown in Fig. 3, panel c. The comparison reveals a poor correlation between our results and previous studies, as well as large variation among the studies themselves, showing total spreads of up to $\Delta \xi = 12$ km s⁻¹. Adding the early supergiants to the picture, the variance is still large, but the correlation to our results improves.

Finally, a comparison of $v \sin(i)$ values is presented in Fig. 3, panel d. The trends are as observed in Paper I towards the higher velocities found here: very good accordance is apparent between our analysis and the set in common with Simón-Díaz et al. (2017), while the results of Fraser et al. (2010) indicate higher values by $\delta v \sin(i) \approx 20\%$ on average. The velocities reported by Smartt et al. (2002) are much higher for two of the three common objects, but the line profiles were matched only by a rotational profile, ignoring macroturbulence unlike in the other studies. Nevertheless, we conclude in this context that overall the agreement between the more recent studies is good.

4.3. Elemental abundances and stellar metallicity

The analysis of elemental abundances of all metal species considered in our sample of stars is summarised in Table 4, featuring the mean abundance, uncertainty and number of analysed lines per species. The last column gives an estimate of the resulting metal mass fraction Z (‘metallicity’), calculated from the available mean abundances derived here. As the abundances derived in this work consider the ten most abundant metal species, these values should give a reliable estimate of the true mass fraction of metals. The error margins listed correspond to the 1σ standard deviation computed from the total set of analysed lines, giving equal weight to each line. These statistical error margins are comparable to those reported in Paper I, though marginally

Table 4. Metal abundances $\varepsilon(X) = \log(X/H) + 12$ and metallicity Z (by mass) of the sample stars.

ID#	Object	C	N	O	Ne	Mg	Al	Si	S	Ar	Fe	Z
1	Sher 25	8.01 (5) ±0.11	8.73 (23) 0.09	8.64 (20) 0.08	8.31 (7) 0.08	7.42 (1) ...	6.35 (4) 0.04	7.81: (8) 0.11	7.47: (6) 0.03	7.53 (8) 0.13	0.016 0.002
2	HD 13854	7.98 (6) ±0.07	8.30 (34) 0.10	8.52 (26) 0.07	8.11 (5) 0.09	7.25 (1) ...	6.17 (4) 0.08	7.76: (10) 0.07	7.33: (3) 0.05	6.45 (1) ...	7.30 (12) 0.09	0.010 0.002
3	HD 14956	7.76 (7) ±0.07	8.70 (27) 0.13	8.53 (16) 0.09	8.08 (8) 0.07	7.37 (1) ...	6.30 (3) 0.05	7.79: (9) 0.09	7.34: (7) 0.05	7.45 (7) 0.11	0.013 0.002
4	HD 91316 ^a	7.94 (11) ±0.08	8.35 (43) 0.08	8.44 (30) 0.08	8.06 (11) 0.06	7.50 (4) 0.29	6.27 (4) 0.03	7.60 (9) 0.09	7.20 (4) 0.05	6.57 (5) 0.04	7.27 (17) 0.09	0.010 0.002
5	HD 114199	8.11 (4) ±0.08	8.45 (19) 0.07	8.53 (20) 0.07	8.24 (4) 0.06	7.46 (1) ...	6.57 (1) ...	7.53 (6) 0.06	7.05 (1)	7.61 (9) 0.09	0.012 0.002
6	HD 152235	8.30 (5) ±0.09	7.85 (22) 0.09	8.70 (27) 0.12	8.15 (8) 0.06	7.39 (1) ...	6.29 (4) 0.06	7.72 (9) 0.15	7.22 (3) 0.03	6.62 (1) ...	7.44 (7) 0.12	0.013 0.002
	CAS ^b	8.35 ±0.04	7.79 0.04	8.76 0.05	8.09 0.05	7.56 0.05	6.30 0.07	7.50 0.06	7.14 0.06	6.50 0.08	7.52 0.03	0.014 0.002

Notes. Uncertainties are 1σ -values from the line-to-line scatter. Numbers in parentheses quantify number of lines analysed. A colon is inserted for abundances with a suspected systematic overestimation (see Sect. 4.3 for details). ^(a) Abundances are only indicative. The second continuum from the companion star needs to be considered for a proper abundance determination, which will result in higher abundances and metallicity. However, this is beyond the scope of the present work. ^(b) cosmic abundance standard (CAS, Nieva & Przybilla 2012; Przybilla et al. 2013)

larger, ranging from ~ 0.05 – 0.15 dex. The number of fitted lines per object and element is typically in the range of 5 to 10 and much larger in some cases, such that standard errors of the mean commonly amount to about 0.02 dex. We omit uncertainty estimations for cases where only one line was suitable for fitting. For the metallicity, the 1σ uncertainty was estimated conservatively to be 0.002 and adopted throughout the entire sample.

The precise determination of atmospheric parameters, abundances and the careful treatment of macroturbulence and rotational broadening permit the production of global synthetic spectra capable of reproducing almost all spectral features found in the observed spectra, including blended lines excluded from our analysis. For Sher 25, a comparison between the observed spectrum and its global solution is discussed and shown in Appendix C, Figs. C.1 to C.9. A similarly close match between model and observation is also found for the other sample stars.

As our sample consists of objects scattered across the Galactic plane with differing distances ρ from the Galactic centre (e.g. ~ 7 kpc for HD 152235 and over 10 kpc for HD 14956) we cannot expect chemical homogeneity because of radial abundance gradients (see e.g. da Silva et al. 2016; Bragança et al. 2019; Arellano-Córdova et al. 2020 for some more recent results). Even so, it can be advantageous to discuss the overall picture in light of the cosmic abundance standard (CAS, Nieva & Przybilla 2012; Przybilla et al. 2008; 2013), which reflects the mean abundances derived for early B-stars in the chemically homogeneous solar neighbourhood (specified at the bottom of Table 4), providing a metallicity $Z = 0.014 \pm 0.002$. Higher metallicities are expected for the sample stars in the inner Milky Way and lower metallicities well beyond the solar circle. Overall, agreement with this expectation is found for the sample stars within the error bars. However, Sher 25 appears to be metal-rich, whereas most of the other stars seem to be offset towards systematically lower metallicities. This is most pronounced for HD 91316 (ID#4), which would result from the presence of significant second light in the binary system (see the discussion in Sect. 5). Second light from a circumstellar disk may also affect the abundance determination of HD 114199 (ID#5).

The metallicity is largely determined by the most abundant metals C, N, O and Ne, so that any systematic metallicity shifts are likely to originate from these. As the atmospheric parameters were derived achieving consistency simultaneously from several

indicators and as they are in overall agreement with literature values, possible systematic abundance uncertainties may potentially stem from imperfections of the model atoms. However, the CNO mixing signatures (see Sect. 4.4) – which are also an indicator for the quality of the atmospheric parameter analysis – are also tightly matched, and the neon abundances are rather high, so no obvious source of the potential metallicity deficit can be identified. The C II $\lambda\lambda 4267$ and $6578/82$ Å lines are notoriously difficult to reproduce reliably (Appendix C) because of their complicated non-LTE line formation (Nieva & Przybilla 2006; 2008). They were consequently ignored for the carbon abundance determination, which relied mainly on the weaker C II lines (e.g. the quartet lines at $\lambda\lambda 5132$ – 5151 Å) that are well reproduced in all cases. Nitrogen abundances were determined from the rich spectrum of N II lines and the oxygen abundances mostly from O II lines, which are around the turning point from major towards minor ionisation stage within the T_{eff} -range investigated here. We note that small systematic underestimates of the abundances of mostly oxygen (and nitrogen when it is highly abundant) within the statistical 1σ -uncertainties suffice to bridge the gap to expected metallicity values.

Among the heavier elements, silicon and sulphur show higher abundances than expected for most stars, with maximum values reached in Sher 25. Lines of S II – which is a minor ionisation stage at this T_{eff} -range – were analysed, as the S III implementation of the model atom of Vrancken et al. (1996) is rather compact with 21 explicit non-LTE terms. Many of the energetically higher terms are also absent in the S II model, which may lead to an overpopulation of the existing terms relative to the true situation and potentially to an overestimated abundance determination. The presence of systematic effects cannot be excluded if only one ionisation stage is considered. A re-investigation using an improved sulphur model atom based on modern atomic data would be required to test this scenario, but this is beyond the scope of the present paper.

The case of silicon is different, as lines from three ionisation stages are present in the observed spectra around the T_{eff} -values investigated here, see Appendix C for the case of Sher 25 and Fig. 4 for a selection of line fits in HD 13854 (ID#2) and HD 14956 (ID#3). Most of the lines from Si II/III/IV – weak and strong alike – are reproduced simultaneously for the same abundance. This leaves little room for imperfections of the model

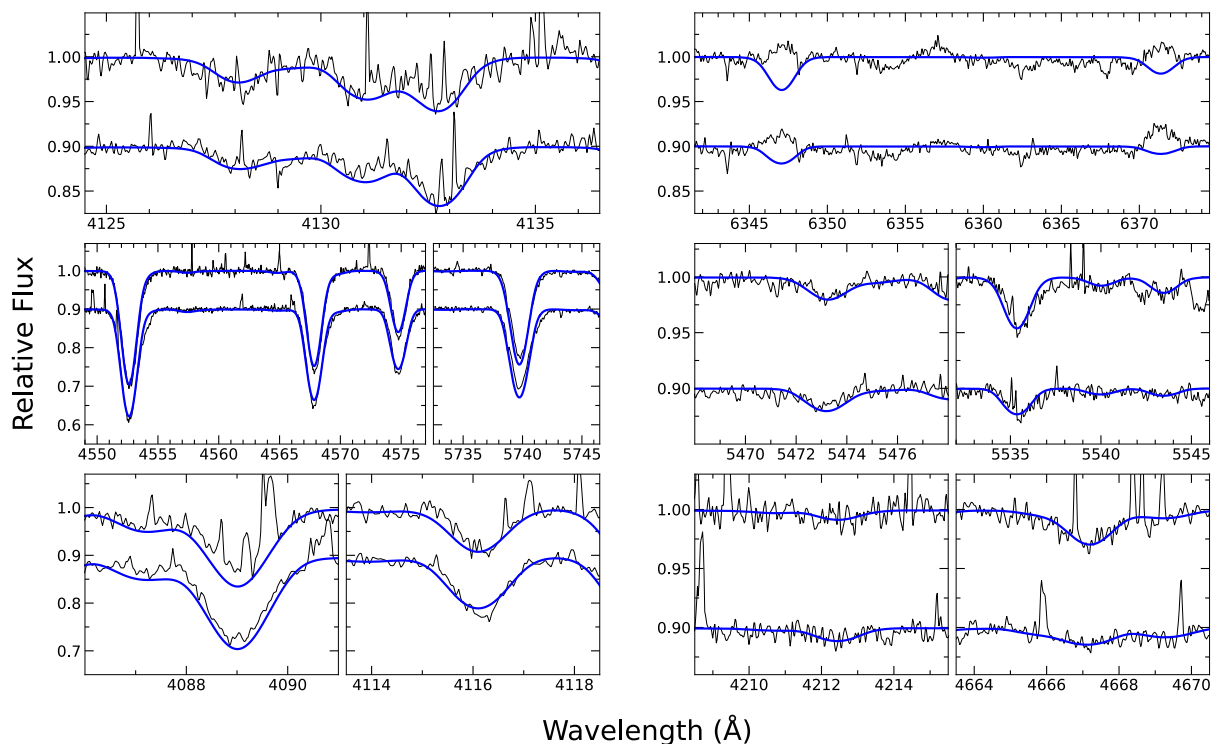


Fig. 4. Comparison of best-fitting models (blue) for observed spectra (black) of HD 13854 and HD 14956 (upper and lower lines in each sub-panel). The three rows show lines of different ionisation stages of silicon: Si II $\lambda\lambda$ 4128 and 4130 Å (upper left), Si II $\lambda\lambda$ 6347 and 6371 Å (upper right); the Si III triplet $\lambda\lambda$ 4552-4575 Å and Si III λ 5739 Å (middle left), Si III $\lambda\lambda$ 5473 and 5540 Å (middle right); Si IV $\lambda\lambda$ 4088 and 4116 Å (lower left), Si IV $\lambda\lambda$ 4212 and 4666 Å (lower right panel).

atom, except for some details. Such are for example the Si II doublet lines $\lambda\lambda$ 6347 and 6371 Å, which are observed in emission but calculated in absorption. The lower level of the transition is radiatively coupled to the Si II ground state, which may make it sensitive to details of the overlap of the corresponding Si II resonance lines with spectral lines of other species⁴, which may drain the lower level's population, thus enabling the emission. We note that analogous calculations with the unified non-LTE model atmosphere code FASTWIND also fail to reproduce the observed emission (M. Urbaneja, priv. comm.), implying that our neglect of sphericity and mass-outflow is not responsible for the failure. On the other hand, the Si III triplet $\lambda\lambda$ 4552-4575 Å is sensitive to mass-loss for very luminous supergiants (see Dufton et al. 2005). Overall, further investigations beyond the scope of the present work are required for the case of silicon to clarify the impact of modelling details on the line formation. The high silicon abundances derived here have to be viewed with caution until then.

4.4. Signatures of mixing with CNO-processed material

The atmospheres of rotating stars can be mixed with CNO-processed matter from the stellar core, facilitated by various physical effects such as meridional circulation or shear-mixing as a consequence of differential rotation (e.g Maeder & Meynet 2012; Langer 2012). The mixing may also be impacted by the presence of magnetic fields. The nitrogen-to-carbon (N/C) and nitrogen-to-oxygen (N/O) abundance ratios sensitively probe the degree of mixing with nuclear-processed material. Tracking stars

⁴ The He I singlet problem (Najarro et al. 2006) in a restricted parameter range of late O-type stars may be seen as an analogue.

in a N/C versus N/O diagram (cf. Fig. 5 of Przybilla et al. 2010) can help to gain insight into the evolutionary status of the examined stars. Moreover, as the graph shows only minor dependence on initial stellar masses, rotational velocities and the details of the mixing mechanisms for small relative enrichment (i.e. by a factor ~ 4 over the initial N/O), it can serve to assess the overall quality of the observational results (Maeder et al. 2014).

Figure 5 shows the ratios of surface abundances for carbon, nitrogen and oxygen (normalised to 'initial' CAS values, see Table 4) for this work's sample stars and a collection of 76 objects analysed with a similar methodology to the one employed here, and three literature results for Sher 25 (see Table 5 and Sect. 6 for a discussion). The diagram also shows the limiting analytical solutions for the CNO-cycle: assuming constant (initial) oxygen abundance in the CN-cycle leads to the upper (almost vertical) boundary function, while the assumption of constant (equilibrium) carbon abundance in the ON-cycle leads to the lower (horizontal) solution. Predictions from stellar evolution calculations generally fall in between these limits, exemplified here by the model track for a rotating $25 M_{\odot}$ star by Ekström et al. (2012).

It is apparent that the bulk of analysed stars show mixing ratios of less than a factor ~ 10 in both N/C and N/O above initial values, constrained tightly on the predicted evolutionary pathway. Four of the present sample stars also fall into this category. While HD 13854 (ID#2) and HD 152235 (ID#6) share very similar spectroscopic and fundamental parameters, the former shows mixing ratios typical for a supergiant at average rotation, whereas the latter features strikingly low CNO enhancement. Normal ratios, compatible with mixing having occurred on the main sequence, are also found for the rapidly rotating Be star HD 114199 (ID#5) and possibly HD 91316 (ID#4).

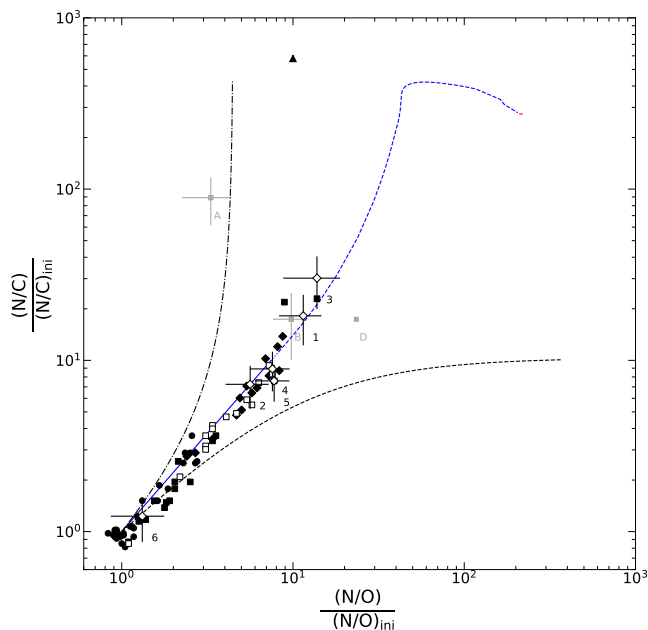


Fig. 5. Nitrogen-to-carbon ratio versus nitrogen-to-oxygen ratio, normalised to initial values. Objects from the present work are shown (open diamonds, marked by their ID#) and from previous work employing an analysis methodology similar to the present one: B-type main-sequence stars (Nieva & Simón-Díaz 2011; Nieva & Przybilla 2012, black dots), BA-type supergiants (Przybilla et al. 2010, black diamonds), B-type supergiants (Paper I, open squares), late O-type main-sequence stars (Aschenbrenner et al. 2023, black squares) and the stripped CN-cycled core γ Columbae (Irrgang et al. 2022, black triangle). For comparison, the development of the surface CNO abundances is shown for a $25 M_{\odot}$, $\Omega_{\text{rot}} = 0.568 \Omega_{\text{crit}}$ model by Ekström et al. (2012). The colour and style of the line depicts the different (main) evolution stages: ZAMS until TAMS (solid blue), further development until beginning of core He-burning (dotted blue), until core He exhaustion (dashed blue) and carbon-burning (red, at the very end of the track). The dashed black and dash-dotted lines depict the analytical boundaries for the ON- and CN-cycle, respectively (cf. Fig. 1 of Maeder et al. 2014). The grey squares are solutions for Sher 25 from the literature, see Sect. 6. Their error bars are from standard errors of the mean CNO abundances, while error bars for results from the present work represent 1σ standard deviations.

Figure 5 also shows stars with significantly more enriched atmospheres ($N/C \geq 20$). Besides the extreme case of the stripped CN-cycled core γ Columbae (Irrgang et al. 2022) towards the top of the figure and two ON-stars with binary mass-overflow history (HD 14633 and HD 201345, described by Aschenbrenner et al. 2023) we also find two stars from the present sample as highly enriched, Sher 25 (ID#1) and HD 14956 (ID#3). While it is in principle feasible to produce such large enhancement for massive, rapidly rotating stars, a potential binary interaction with mass exchange has to be taken into consideration. In all cases, a detailed study of each individual star’s unique characteristics aids in understanding the measured CNO signature (see Sect. 5 for a discussion of each of our comparison stars and Sect. 6 for an in-depth account of the status of Sher 25).

4.5. Spectroscopic distances

The comparison of spectroscopic distances (determined in analogy to Paper I) with those inferred from Gaia EDR3 parallaxes (photogeometric distances of Bailer-Jones et al. 2021) is shown in the upper panel of Fig. 6, while the lower panel shows the relative differences. The figure also depicts stars discussed in Pa-

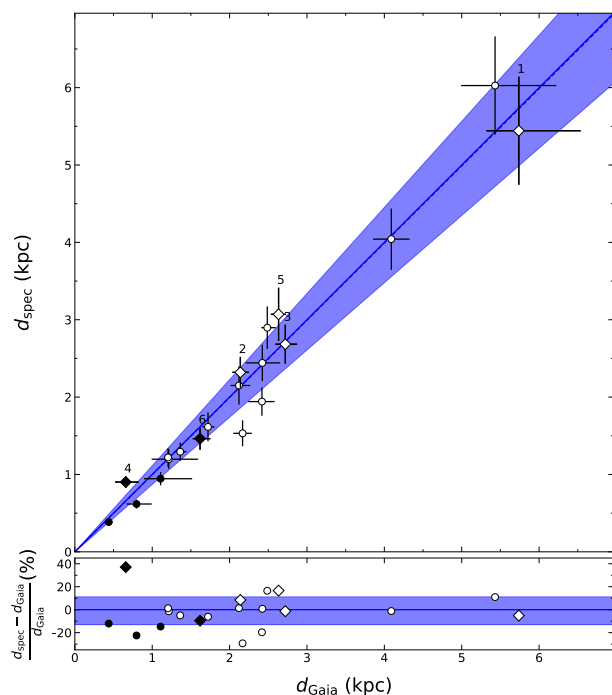


Fig. 6. Comparison of derived spectroscopic distances and distances based on Gaia EDR3 parallaxes (*upper panel*) and their relative differences (*lower panel*). Diamonds represent the objects analysed in this work, while dots correspond to those of Paper I – filled symbols are used to depict objects with RUWE values > 1.3 . The solid blue lines depict equivalence, while the dashed line shows the best linear fit to the data. The shaded area marks the region of 1σ standard deviation from the mean. In the fit, only data with good RUWE values were employed, that is the open symbols.

per I, providing a comprehensive overview to the overall quality of the correspondence between measurements across the entire domain of B-type supergiants. For the sub-sample of objects which can be compared reliably, that is, those with small renormalised unit weight error (RUWE < 1.3), the relative differences show a mean offset of $\mu_s = -1\%$ with a sample standard deviation of $\sigma_s = 12\%$. The hot supergiants analysed in this work spread over a range in distance from 1 to about 5 kpc (Sher 25 being the most distant star of the sample), resembling the range of values of the entire sample.

Evidently, the relationship shows no noticeable deviations either on the near or the far end of the distance scale. For IDs#1, 2, 3, and 6, the accordance is good, with relative differences to the parallactic distance less than 10%. Specifically, for HD 13854 (ID#2) the spectroscopic distance is further corroborated by the star’s membership in the open cluster NGC 869 ($d_{\text{NGC869}} \approx 2.3$ kpc, Currie et al. 2010). Notable deviations exist only for two of the sample stars: for HD 91316 we derive a distance of 900 ± 70 pc, barely compatible with its parallax-based estimate of 660^{+170}_{-140} pc (at a RUWE of 2.46). Even worse agreement is achieved with the star’s Hipparcos distance of 1670^{+710}_{-380} pc (van Leeuwen 2007). For HD 114199 the deviation is less extreme (but considerable) with our estimate of 3070 ± 340 pc being about 17% above the Gaia value of 2630 ± 100 pc (RUWE = 0.786). In the case of both of these objects the broader picture of their deduced characteristics hint at peculiarities in their evolutionary history, which are able to explain the observed discrepancy in distances, and we refer to Sect. 5 for an in-depth discussion. Ex-

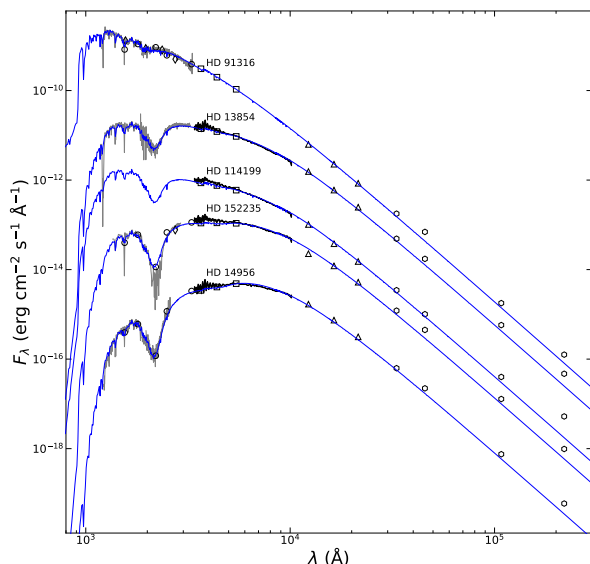


Fig. 7. Spectral energy distributions of the sample stars. ATLAS9-SEDs, normalised in V and reddened according to values from Table 3 (blue lines) are compared to IUE and Gaia spectrophotometry (grey and black lines, respectively) and photometric data in various wavelength bands: ANS (circles), TD1 (diamonds), Johnson (squares), 2MASS (triangles), and ALLWISE data (hexagons). For better visibility, the SEDs and photometry for HD 152235 and HD 14956 were shifted by -2 and -3 dex, respectively.

cluding them, it is clear that the resulting distances in the present work maintain the overall good agreement reported in Paper I.

4.6. Characterisation of the ISM sight lines

While the methodological approach remains identical to the one described in Paper I, the determination of the reddening law for this work's sample made use of additional data, as summarised in Sect. 2. Here, the ISM sight lines towards the comparison stars will be discussed. We refer to Sect. 6 for the case of Sher 25, where additional constraints will be considered.

Figure 7 shows the data and best-fitting model SEDs for the comparison stars, ordered by increasing colour excess $E(B - V)$ from top to bottom. For most objects, the model SED can explain all available (spectro-)photometric data sufficiently, though some ambiguities and mismatches must be explained. We see that for all objects the WISE band W4, and to a lesser extent also W2, show significant excess flux. While it is possible to reproduce those features assuming dust emission lines or, as in the case of HD 114199, a black body contribution from an indistinct disk around the star, these assumptions barely change the resulting reddening parameters. We consequently omit these data-points in the fitting process. In the case of HD 152235 the IUE spectrum shows excess absorption in the $\lambda 2175 \text{ \AA}$ extinction bump, not present in the ANS data. To fit the former would require the employment of an anomalous reddening law, while the latter can be consistently fit with all other measured data – we therefore prefer the ANS data over the IUE spectrum (which is very noisy at these low flux levels). We also note that while the Gaia spectrophotometry is reproduced well overall, some deviations occur at the borders of the coverage. At the high wavelength limit a steep drop of the flux is observed at a few wavelength points, likely an issue from the calibration. In analogy, the Gaia spectrophotometry also overestimates the fluxes between the U and B bands, a known issue described in Sect. 8.2 of Montegriffo

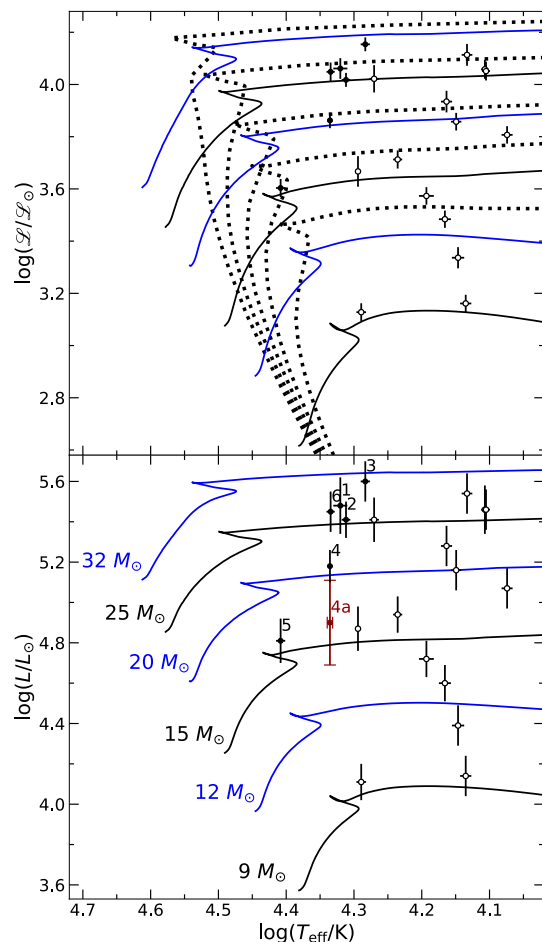


Fig. 8. Location of the sample objects (black dots with error bars) and B-type supergiants analysed in Paper I (open symbols) in two diagnostic diagrams, the sHRD (*upper panel*) and the HRD (*lower panel*). For comparison, loci of evolution tracks for stars rotating at $\Omega_{\text{rot}} = 0.568 \Omega_{\text{crit}}$ (Ekström et al. 2012) are indicated for various ZAMS-masses. Isochrones for the model grid, corresponding to ages of $\log \tau_{\text{evol}} \in \{6.75, 6.85, 6.95, 7.05, 7.20\}$ are depicted as dotted lines in the upper panel (increasing in age from top to bottom). For HD 91316 the luminosity as derived from the parallactic distance (ID#4a in Table 3) is depicted with a red symbol and marked accordingly. Error bars indicate 1σ uncertainty ranges.

et al. (2023), see also their Fig. 38. On the other hand, the Johnson and ANS photometry and the IUE spectrophotometry can be nicely matched by the reddened models.

The derived values for R_V and $E(B - V)$ of the comparison stars are comparable in range to the ones of Paper I with both low and high values realised (see Table 3). For R_V , they vary between 2.7 to 3.2, while for the colour excess values range from about $E(B - V) = 0.1$ to 0.8 mag.

4.7. Evolutionary status

Tracks of stellar evolution models can be used to derive the current evolutionary status of the sample objects. For this purpose we utilise two related diagnostic diagrams in Fig. 8: the spectroscopic HRD (sHRD, $\log(L/L_\odot)$ versus $\log T_{\text{eff}}$, introduced by Langer & Kudritzki 2014) and the HRD ($\log L/L_\odot$ versus $\log T_{\text{eff}}$). While the stars' positions in the sHRD are determined by the spectroscopic solution alone ($L = T_{\text{eff}}^4/g$), the loci in the 'classic' HRD also rely on the objects' distance and reddening.

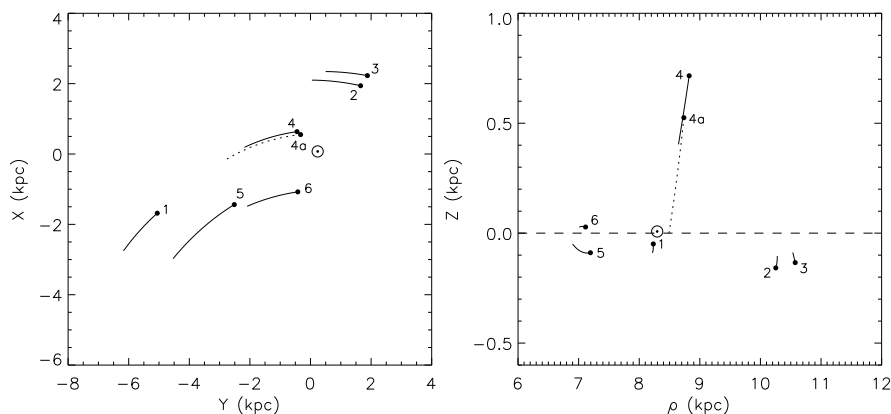


Fig. 9. Visualisation of the kinematics of the sample stars in the Galactic potential. Galactic Cartesian coordinates XYZ are employed, with the origin shifted to the position of the Sun, adopting its galactocentric distance from the Gravity Collaboration et al. (2019). *Left panel:* galactic plane projection. *Right panel:* meridional projection. ρ is the galactocentric distance and the Galactic mid-plane is indicated by the dashed line. Black dots mark the current positions of the stars, the curves show the trajectory calculated backwards in time according to the evolutionary age (see Table 3). The alternative solution ID#4a (dotted line) was calculated backwards until the Galactic mid-plane was reached, about 13 Myr ago.

ing law. In addition to the present sample stars the cooler B-type supergiants from Paper I are also shown in Fig. 8⁵, together with evolutionary tracks and isochrones for rotating stars (Ekström et al. 2012). The present sample stars, with half of them belonging to luminosity class Iab, are on average more massive and more luminous than those of Paper I (about half belong to luminosity class Ia), reflecting the existence of much more luminous supergiants than discussed here on the hot side of the Humphreys-Davidson limit (Humphreys & Davidson 1979).

Our present sample stars had ZAMS masses between about 15 and 30 M_{\odot} (but see also the discussion of HD 91316 (ID#4/4a) in Sect. 5). The stellar ages range between about 6.5 to 11 Myr, again with the exception of HD 91316. It has to be stated that the masses and ages were derived assuming that the rotation rates employed for the computation of the evolutionary tracks and isochrones are representative on average for the sample. Systematic shifts in mass and age result if the initial rotational velocities had other values, but we expect them to be covered by our uncertainties in most cases. The projected rotational velocities of the sample stars are slightly higher than in Paper I, in agreement with predictions (Ekström et al. 2012) for slightly earlier evolutionary stages. Only HD 114199 rotates significantly faster, in accordance with its earlier evolutionary stage and its Be star nature. Another issue for the comparison between observation and models can be metallicity. The value of $Z = 0.014$ employed by Ekström et al. (2012) is representative for the solar neighbourhood, but stars at lower or larger galactocentric radius will experience the effects of abundance gradients. One can therefore expect metallicities to vary a bit among the sample stars (see the discussion in Sect. 4.3). However, the $Z = 0.014$ tracks can still be viewed as representative because the closest published Geneva tracks for higher and lower metallicity are for $Z = 0.020$ (Yusof et al. 2022) and 0.006 (Eggenberger et al. 2021), that is very distant in metallicity space. Moreover, the evolutionary tracks remain similar throughout this metallicity range (see e.g. Yusof et al. 2022, their Fig. 5).

The overall good agreement of the stars' positions in both the sHRD and HRD relative to the evolutionary tracks indicates that the sample supergiants are on their first crossing of the HRD towards the red. Otherwise, the high mass-loss experienced during the RSG phase would yield different positions, as also likely in the case of binary evolution – as for HD 91316.

⁵ Note that in the analogous Fig. 15 of Paper I the uncertainties for those sample stars (marked by open symbols here) in the sHRD were also adopted for the HRD, which we correct here.

4.8. Kinematics

It may be useful to consider trajectories in the Galactic potential for some stars to further constrain their evolutionary status from flight times. The Galactic potential as described by Allen & Santillan (1991) together and the code of Odenkirchen & Brosche (1992) were employed to calculate the Galactic orbits of the sample stars. Coordinates (α , δ) and proper motions (μ_{α} , μ_{δ}) in right ascension and declination and radial velocities for HD 13854 (ID#2), HD 14956 (ID#3) and HD 91316 (ID#4/4a) were adopted from Gaia DR3 Gaia Collaboration (2022), spectroscopic distances (and d_{Gaia} for solution ID#4a) from Table 3 and radial velocities from Hendry et al. (2008) for Sher 25 (ID#1)⁶, from Gontcharov (2006) for HD 152235 (ID#6) and a value of -45.6 km s^{-1} for HD 114199 (ID#5) as determined from the observed spectrum. Figure 9 shows the resulting stellar trajectories in the Galactic plane and the meridional projection. Stars IDs#1, 5 and 6 are consequently located in the Carina-Sagittarius spiral arm and stars IDs#2 and 3 in the Perseus spiral arm. For all sample stars the kinematics is dominated by the rotation around the Galactic centre (at Galactic Cartesian coordinates $X = -8.178 \text{ kpc}$, $Y = 0 \text{ kpc}$, $Z = 0 \text{ kpc}$ in this visualisation), except for HD 91316 (ID#4/4a). The star shows a clear runaway movement from its origin in the local spiral arm perpendicular to the Galactic plane, which explains its high galactic latitude. The implications for the evolutionary scenario of HD 91316 will be discussed in the next Section.

5. Summary of individual comparison stars

HD 13854 (ID#2). This is one of the supergiant members of the open cluster NGC 869 (h Per) in the Per OB1 association. It shows a CNO mixing signature that one may expect for a 'typical' supergiant of its mass at average rotation, see Fig. 5. Its metallicity is lower than the standard value in the solar neighbourhood, as is expected from its position farther out in the Galactic disk. Other than this, it is the closest analogue to Sher 25 among all the sample stars discussed here because of its very similar atmospheric and fundamental stellar parameters.

HD 14956 (ID#3). The star is a member of the Per OB1 association. It is the most massive star of the entire sample, including the objects from Paper I. HD 14956 shows the highest degree of CNO-mixing in Fig. 5, except for the stripped-core star γ Col (Irrgang et al. 2022). The position in the N/O-N/C diagram in conjunction with only a mild enrichment of helium

⁶ Systematic velocity, as the star is known to show radial velocity variations, possibly due to pulsations (Taylor et al. 2014).

could be reached already after termination of the main-sequence phase, if such a massive star was rotating somewhat faster than average (cf. the evolutionary tracks of Ekström et al. 2012). Predictions for a post-RSG scenario would locate the star close to the turning point immediately preceding the Wolf-Rayet phase in Fig. 5, with the CNO abundances dominated by convective dredge-up, irrespective as to whether the star was rotating or not. Values of $\gamma \approx 0.2$ and a surface gravity lower by a factor two would be expected, which are not observed. We note, however, that the position of HD 14956 in Fig. 5 is similar to that reached by the two ON stars HD 14633 and HD 201345 discussed by Aschenbrenner et al. (2023), which have obtained their high degree of CNO mixing by mass accretion in a binary scenario. HD 14956 was identified as a SB1 system with a period of ~ 175 days by Abt & Levy (1973), but see also de Burgos et al. (2020).

HD 91316 (ρ Leo, ID#4). The star is one of the few supergiants at high galactic latitude ($\ell \approx +53^\circ$), a position reached as a run-away star. Figure 9 shows its trajectory in the Galactic potential. Solution #4, adopting the spectroscopic distance, is obviously unable to trace the star back to a star-forming region close to the Galactic mid-plane – where massive stars are born – within the lifetime of the deduced $\sim 20 M_\odot$ star. The Gaia DR3 distance is, on the other hand, significantly shorter, leading to a lower luminosity and therefore to a smaller mass and longer lifetime (solution #4a). This may suffice to bring the trajectory back to the galactic mid-plane within 13 Myr, which may be compatible with a dynamical ejection from the birth cluster shortly after formation. However, the result is a discrepancy between the position of the star relative to evolution tracks in the sHRD (determined by solution #4) on the one hand and the HRD (determined by the Gaia parallax, #4a) on the other (~ 16 to $17 M_\odot$). Moreover, the calculation of the mass from Eq. 3 of Paper I and adopting the Gaia distance, yields a third mass value of $\sim 11 M_\odot$ (though with large error margins). The latter may require non-standard evolution. Overall, no consistent picture is obtained.

A hint for a solution may come from the high Gaia DR3 RUWE value of 2.457 for ρ Leo, implying the parallax not to be reliable and pointing towards a possible binary nature. The star lies close to the ecliptic, such that occultations by the moon occur, which can be exploited to verify the binary hypothesis. A first investigation by de Vegt & Gehlich (1976) found ρ Leo to be a close double star with a projected separation of $\rho = 2.9 \pm 0.1$ mas and a magnitude difference of 0.04 ± 0.09 mag (at position angle $276^\circ.5$). On the other hand, Evans & Edwards (1981) found no duplicity and Radick et al. (1982) reported ρ Leo as a possible binary with $\rho = 10.3 \pm 0.8$ mas and a magnitude difference of 1.07 ± 0.23 mag in the V band (at a position angle of $109^\circ.1$). ρ Leo was resolved more recently by speckle interferometry using a H α filter, finding the companion at a position angle of $98^\circ.3 \pm 7^\circ.7$ at a separation $\rho = 46.1 \pm 1.8$ mas, with a brightness difference of 1.5 mag (Tokovinin et al. 2010). The authors noted that a SB subsystem is suspected. Levato et al. (1988) concluded that the star is radial velocity variable, see their discussion for the long history of measurements (note that ρ Leo shows non-radial oscillations), whereas Chini et al. (2012) even characterised the star as SB2 on the basis of two spectra, but without giving further details. A binary solution would explain the unusual pure absorption profile of H α observed for ρ Leo, unlike the other B1 Iab supergiants in Fig. 2 which show P-Cygni profiles. Two lower-mass weak-wind stars of very similar spectral type would be required to remain inconspicuous in the SED (Fig. 7), closely aligned in radial velocity and showing similar rotational veloc-

ities. The presence of two continua would weaken the spectral lines, letting the Balmer lines appear narrower (thus yielding a Iab classification) as they in fact are and giving lower chemical abundances as are indeed present.

A further piece of the puzzle is the rotation period of 26.8 d deduced from a 80 d K2 lightcurve (Aerts et al. 2018). From a comparison of v_{rot} (assuming a reasonable radius for the primary) and $v \sin i$ means that the system is seen not too far from being equator-on. The orbital motion is also likely to be co-aligned, with the major axis roughly lying in the East-West direction based on the position angles cited above. In the absence of a reliable parallax, magnitude difference and separation of the components' lines⁷ no firm conclusions on the binary system can be drawn. But we may make some estimations guided by the available data. Assuming a distance of 700 pc and a magnitude difference of the components of 1.5 mag, luminosities of $\log L/L_\odot \approx 4.85$ and $\log L/L_\odot \approx 4.25$ would result, indicating a supergiant primary of about 16 to $17 M_\odot$ and a secondary of about $11 M_\odot$ close to the TAMS. Such a configuration would be able to reach the current position high above the galactic plane within the lifetime of the supergiant, assuming dynamical ejection early after formation. A highly eccentric orbit with the above orientation could explain the detection or absence (when the two stars are too close) of the second source at particular times, it would naturally explain a very low relative radial velocity difference of both stars and only at periastron would the two line systems perhaps be separated enough for identification. A highly eccentric orbit would also disfavour mass exchange between the two components.

With the rough sketch of the binary nature we can only stress that the stellar parameter and abundance solutions for the star as summarised in Tables 3 and 4 provide a rough indication of the true values. In particular the abundances will be underestimated. Further monitoring of ρ Leo is certainly needed to constrain the orbit and the properties of the binary components.

HD 114199 (ID#5). The reclassification of HD 114199 from supergiant to a bright giant Be star based on spectral morphology was already discussed in Sect. 2. It shows a pronounced CNO mixing signature (Fig. 5) which is expected for a massive fast rotator – it can actually be expected to rotate faster than the models with initial angular velocity of $\Omega_{\text{rot}} = 0.568 \Omega_{\text{crit}}$ discussed by Ekström et al. (2012), see Georgy et al. (2013) for such models, which, however, terminate at masses slightly below that of HD 114199. A systematic underestimation of the star's initial angular velocity and correspondingly lower mass (see our discussion in Sect. 4.7) may also explain the discrepancy between compared distances. Even a small reduction of the star's mass (e.g. by $1 M_\odot$) brings our estimation well within the mutual uncertainty limits with the parallactic value. Its position in the (spectroscopic) HRD (Fig 8) likely corresponds to the star being on the blueward-evolving part of the track very close to the TAMS. Consequently, HD 114199 may still be in its core H-burning phase, unlike the other stars of our sample.

HD 152235 (ID#6). The star is a member of the massive star cluster NGC 6231 in the Sco OB1 association, its age being commensurate with the cluster age of 4-7 Myr (Sung et al. 2013, derived using Ekström et al. tracks for rotating stars). It was identi-

⁷ Several spectra of ρ Leo are available in the CFHT and ESO archives from different instruments, but they do not show SB2 character. The data of Chini et al. (2012) showing two line systems would be pivotal in this context to analyse both components, e.g. using our methodology in analogy to Irrgang et al. (2014) or González et al. (2017; 2019).

Table 5. Literature values for atmospheric parameters and elemental abundances of Sher 25.

ID #	T_{eff} (kK)	$\log g$ (cgs)	y (by number)	ξ (km/s)	$\log(X/H) + 12$					code	source
					C	N	O	Mg	Si		
A	22.3±1.0	2.60±0.10	0.10±0.02	15	7.01±0.06	8.42±0.12	8.87±0.07	7.46	7.42±0.07	TLUSTY/H+He	Smartt et al. (2002)
B	21.5±1.0	2.60±0.20	...	20	7.82±0.16	8.52±0.09	8.50±0.03	7.59±0.36	7.40±0.20	TLUSTY	Hendry et al. (2008)
C	22.0±1.0	2.60±0.15	...	23	...	8.74±0.15	8.51±0.05	...	7.61±0.08	FASTWIND	Hendry et al. (2008)
D	21.0±1.0	2.50±0.20	...	15	7.8	8.5	8.1	CMFGEN	Hendry et al. (2008)
I	20.9±0.5	2.61±0.06	0.117±0.015	16±2	8.01±0.05	8.73±0.02	8.64±0.02	7.42	7.81±0.04	ADS	this work

Notes. Abundance uncertainties for the metals are standard errors of the mean, as provided in the literature.

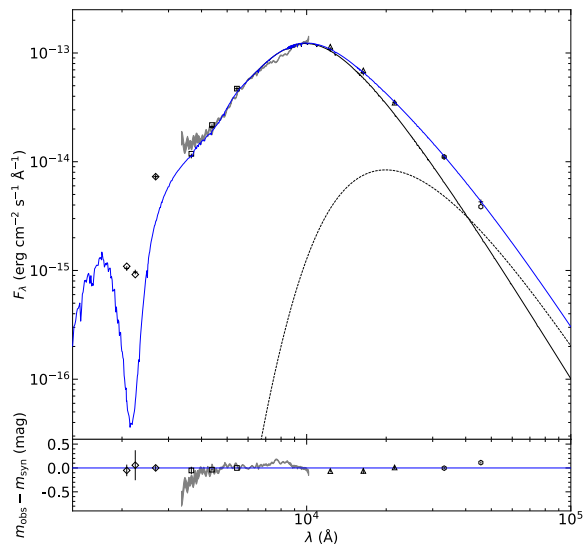


Fig. 10. Spectral energy distribution of Sher 25. A comparison of the reddened model flux (solid blue line) to photometric and spectrophotometric measurements (*upper panel*) and the difference between modelled and observed parameters measured in magnitudes (*lower panel*) are shown. A blackbody contribution (black dashed line) with a temperature of $T = 1800$ K is assumed in addition to the stellar SED (black solid line). The grey line depicts Gaia spectrophotometry. Symbol assignment is the same as in Fig. 7. In addition, near-UV Swift/UVOT photometric measurements (diamonds) are shown. Results of synthetic photometry on the model SED in the respective pass bands are also indicated (plus signs). The error bars in the lower panel depict the 1σ uncertainty range.

ified as an X-ray source (Kuhn et al. 2017). This supergiant shows stellar parameters close to those of Sher 25 and HD 13854, but is remarkable for its low CNO mixing signature. One may suppose it to stem from a slowly-rotating main-sequence progenitor. However, if one scales its $v \sin i$ value to the star’s ZAMS radius assuming angular momentum conservation, an initial rotational velocity of at least 350 km s^{-1} is deduced. A possible scenario to solve the conundrum may be that the supergiant is located in a binary system with large enough separation during the main-sequence evolution to avoid tidal interactions, so that the star may have indeed been a slow rotator initially. Main-sequence stars in detached eclipsing binaries are known to show CNO abundances close to pristine values (Pavlovski et al. 2023). The expansion to giant and supergiant dimensions may then have allowed tides to become effective, spinning up the stellar envelope. Detection of a companion and detailed binary modelling would be necessary to prove the validity of such a scenario, which is beyond the scope of the present paper. However, we note that an indication for a presence of a binary companion is given by a Gaia DR3 RUWE value of 1.357 for HD 152235.

6. Discussion of Sher 25

The present analysis of Sher 25 finds similar atmospheric parameters to previous work that employed different non-LTE codes, as summarised in Table 5. On the other hand, abundance values for the five elements studied so far showed a large scatter and seem strongly model dependent. Note that deviating from our usual notation, abundance uncertainties in Table 5 are standard errors of the mean, as provided in the literature. Our present values for CNO abundances show a high nitrogen enrichment and a depletion of both carbon and oxygen, relative to CAS values that should be representative for the initial CNO abundances because Sher 25 is located at a similar galactocentric radius as the solar neighbourhood. However, in contrast to some previous analyses – which found a similar pattern – our values together with solution B align closely to the predicted mixing path in the N/O–N/C diagram (Fig. 5). Solution A from Table 5 provides a locus beyond the analytical CN-process boundary, while solution D is inclined towards ON-processing. Solution C is not discussed in this context, as no carbon abundance was provided. Concerning the heavier species, we recall that our silicon abundance is possibly overestimated (see Sect. 4.3).

An analysis of Sher 25 and its hourglass nebula requires an understanding not just of the star itself, but also of its environment. Since this means understanding its relationship with the massive cluster NGC 3603, we have to accurately characterise the complex sight line towards Sher 25 to precisely define its spectroscopic distance. Again, fits to the the observed SED are employed, which is shown in Fig. 10. Valuable UV photometry from the UVOT instrument on board the Swift mission are available (the available measurements in the UVW1, UVM2 and UVW2 bands were averaged) in addition to optical and IR photometry, and the spectrophotometry from Gaia. A comparison between observed and synthetic magnitudes is explicitly made. The synthetic photometry is based on filter curves and effective wavelengths adopted from the SVO Filter Profile Service⁸ (Rodrigo et al. 2012; Rodrigo & Solano 2020). The lower panel of Fig. 10 shows the residuals.

Good agreement between the model and observations is found for wavelengths below $\sim 10^4 \text{ \AA}$ for $E(B - V) = 1.66 \pm 0.03$ and $R_V = 3.4 \pm 0.1$ ⁹, except for the Gaia spectrophotometry towards the blue and red limits (as also found for the comparison

⁸ <http://svo2.cab.inta-csic.es/theory/fps/>

⁹ For comparison, Smartt et al. (2002) adopted $E(B - V) = 1.6$ and $R_V = 3.7 \pm 0.5$, and 6.3 ± 0.6 kpc for the distance. Hendry et al. (2008) employed the data of Melena et al. (2008), who found a two-component reddening law with $E(B - V) = 1.1$ and $R_V = 3.1$ for the foreground and $E(B - V) = 1.39$ and $R_V = 4.3$ within the cluster, adding up to a total extinction of $A_V = 3.1 \times 1.1 + [(E(B - V) - 1.1) \times 4.3] = 4.657$, and a distance of 7.6 kpc. An overview of previous reddening and distance data toward NGC 3603 can be found in Table 4 of Melena et al. (2008) and in Table A.1 of Maíz Apellániz et al. (2020).

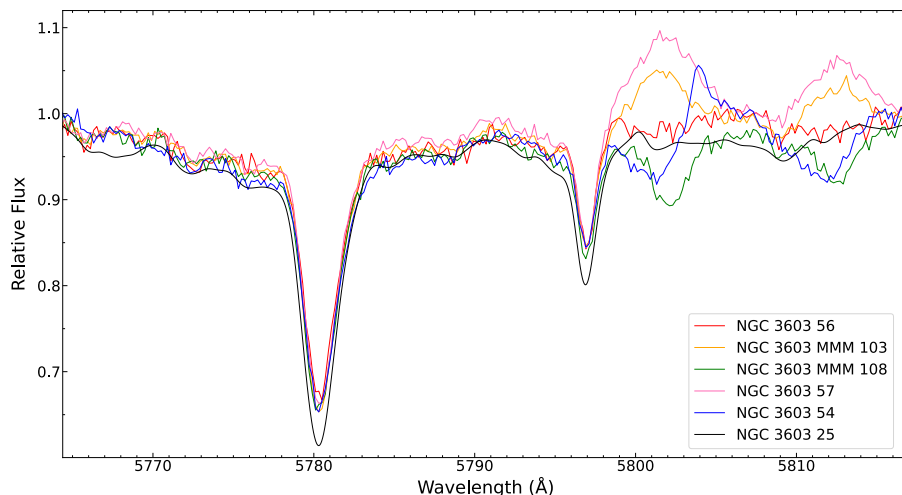


Fig. 11. Spectra of Sher 25 and of five NGC 3603 bona-fide O-type cluster stars in the region of the two deep and narrow diffuse interstellar bands (DIBs) $\lambda\lambda 5780$ and 5797 Å, see the legend. Other DIBs in this wavelength range are the shallow but broad $\lambda 5778$ Å feature and the narrow and shallow $\lambda\lambda 5766$, 5772 , 5776 , 5793 , 5795 and 5809 Å features. The variation of the different spectra in the red is due to the different appearance of the stellar C iv $\lambda 5801$ and 5812 Å lines in the O-type stars. The spectrum of Sher 25 was artificially downgraded in resolution to match the lower $R = 5800$ of the FLAMES/GIRAFFE data.

stars). On the other hand, the stellar SED (solid black line) is clearly insufficient to explain the marked observational IR excess (present in the J , H , and K filters, as well as the WISE bands), which is also indicated by the IR glow in the area visualised in Fig. 1. This discrepancy can be removed by introducing a blackbody (BB) emitter with a temperature of $T = 1800$ K (dashed line in Fig. 10), the nature of which cannot be constrained here. As such a BB emitter is necessary in order to reproduce the IR excess of some O-type stars in NGC 3603 as well (see Appendix A), it appears to be connected to NGC 3603, and not a circumstellar feature. It may be due to hot dust, at the limiting temperature for sublimation of graphite grains, the most stable dust species.

This constrains our spectroscopic distance of Sher 25 to $d_{\text{spec}} = 5440 \pm 700$ pc, whereas the Gaia-based distance is $d_{\text{Gaia}} = 5740^{+800}_{-420}$ pc, with a RUWE value of 0.943 indicating a reliable value. As discussed in detail in Appendix B, this location could put Sher 25 in principle in the vicinity of NGC 3603, which was calculated to lie at a distance of $d_{\text{NGC3603}} = 6250 \pm 140$ pc. However, the sheer existence of the hourglass nebula requires Sher 25 to be distant enough in the radial direction for this fragile structure not to be exposed to the strong winds of the WR- and early O-star population of NGC 3603. These stars have cleared the surrounding ISM in the lateral direction to larger distances than Sher 25 is located from the cluster core in projection and they have sculpted the pillar out of the molecular cloud in the south-eastern direction (see Fig. 1) at even larger lateral distance. A foreground location of Sher 25, as suggested by our spectroscopic solution, is therefore more likely.

A second approach towards a clear understanding of the relationship between the cluster and Sher 25 may be attempted by looking at information contained in lines of interstellar absorption. Figure 11 shows the wavelength region around 5790 Å, which includes two of the strongest narrow diffuse interstellar bands (DIBs). In fact, practically the entire wavelength region, which for a normal B1 supergiant would be void of stellar lines (except for N II $\lambda 5767.4$ Å in N-rich objects, such as in Sher 25), is dominated by DIB absorption because of the high extinction along the sight line. This includes in particular the shallow but very broad DIB $\lambda 5778$ Å and a number of other features ($\lambda\lambda 5766$, 5772 , 5776 , 5793 , 5795 and 5809 Å) which are shallow and narrow. The plot also shows spectra of five O-type stars, assumed to be members of NGC 3603, taken with the GIRAFFE spectrograph of the VLT/FLAMES facility (Pasquini

et al. 2002). Note that the FEROS spectrum of Sher 25 was artificially downgraded here to match the $R = 5800$ of the GIRAFFE data. In particular, the two strongest DIBs at $\lambda\lambda 5780$ and 5797 Å distinctly show the disparity in strengths between Sher 25 on the one hand and the cluster members on the other: stars assumed to belong to NGC3603 show a consistently lower amount of DIB absorption. This is in spite of the variation in reddening (the values fall in the range $E(B - V) = 1.30 - 1.42$, see Melena et al. 2008) and spread in angular distance θ from the cluster centre (i.e. $\theta \approx 8''$ east for NGC 3603 MMM 108 to $\theta \approx 25''$ west for NGC 3603 54). While this finding maintains our conclusion that the star is clearly not associated with the cluster, on a first glance it may contradict the localisation in the foreground. One may argue that Sher 25 should be located in the background of the cluster. However, what is required is a higher column density of DIB carriers to produce the stronger DIBs, which in addition to a longer path length may also be achieved by having a surplus of DIB carriers located in the circumstellar medium around Sher 25 (which would have interesting implications). Further investigations are certainly required, but are beyond the scope of the present work. In view of the previous discussion we therefore maintain our conclusion that Sher 25 is not associated with NGC 3603 and likely stands in the foreground of the cluster.

A distinct spatial separation of Sher 25 from NGC 3603 is also indicated by the spectra of the circumstellar hourglass nebula of Sher 25 and of the H II region surrounding NGC 3603. We refer to the analysis of the two nebular sites presented by Hendry et al. (2008), using the 'direct' method (e.g. Skillman 1998). The cluster NGC 3603 is one of the most massive very young ($\sim 1 - 2$ Myr) star clusters known in the Milky Way. It is dominated by the light of early O-type stars and four WN6h stars, which provide a harsh UV radiation field that leads to high excitation in the surrounding giant H II region. This gives rise to strong [O III] $\lambda\lambda 4959$ and 5007 Å emission, with the intensity of the weaker component showing about twice the flux of H β , see Figs. 4 and 5 of Hendry et al. (2008). This high excitation is much weaker in the spectra of the hourglass nebula, with [O III] showing only $0.6 \times$ the flux of H β , despite Sher 25 being closer in lateral projection to the cluster core than the H II clouds investigated by Hendry et al. (2008) and despite the regions having about the same oxygen abundance. Instead, the spectrum of the hourglass nebula shows stronger lines from lower-excitation species. In consequence, Sher 25 is not located physically close to NGC 3603, but must be sufficiently separated in the radial direction to avoid exposure to the cluster's UV radiation field

Table 6. Comparison of nebular and photospheric abundances.

Object	$\log(X/H) + 12$				
	N	O	Ne	S	Ar
H II region ^a	7.47±0.18	8.56±0.07	8.11±0.09	7.22±0.22	6.44±0.08
hourglass ^a	8.91±0.15	8.61±0.13	8.46±0.21	...	6.70±0.17
Sher 25 ^b	8.73±0.09	8.64±0.08	8.31±0.08	7.47±0.03	...

Notes. ^(a) Hendry et al. (2008) ^(b) this work

(i.e. at a position in front of the cluster as deduced above). Adopting our spectroscopic distance and extinction value, the luminosity of Sher 25 becomes $\log L/L_{\odot} = 5.48 \pm 0.13$, which for a single star scenario (assuming evolutionary tracks for rotating stars from Ekström et al. 2012) corresponds to a star with $\sim 27 M_{\odot}$ on the ZAMS. The age of Sher 25 is ~ 7 -8 Myr, about four to eight times the age of NGC 3603.

A comparison of nebular abundances for the NGC 3603 giant H II region and the hourglass nebula, as well as of the photospheric abundances of Sher 25 is made in Table 6. The distance of NGC 3603 to the galactic centre is similar to that of the solar neighbourhood. As a consequence one would expect the giant H II region abundances to be close to CAS values (Table 4). Indeed, the heavier species Ne, S and Ar show such agreement, whereas N and O appear underabundant by ~ 0.2 – 0.3 dex. The origin of the latter in particular is not clear, but we note that some assumptions also had to be made for the nebular abundance determination (see Hendry et al. 2008 for details), such that additional unaccounted systematic uncertainties may need to be considered. The abundances of Sher 25 and the hourglass nebula are consistent within the error bars, with stellar ratios for $N/C \approx 5.2$ and $N/O \approx 1.2$ (by number). Besides the high degree of CNO-cycling, the hourglass nebula appears to show increased abundances of neon (also present in Sher 25) and of argon.

Finally, the origin of the hourglass nebula needs to be addressed. In terms of evolutionary stage, Sher 25 is unlikely to have gone through a previous RSG phase according to its CNO mixing signature, as convective dredge-up would have brought the star to the top of the theoretical mixing signature curve in the single-star evolutionary scenario in Fig. 5, in analogy to the discussion of HD 14956 (ID#3) in the previous section. As a result, Sher 25 has expelled the hourglass nebula during its BSG phase with a dynamical age of about 6600 yr (Brandner et al. 1997a). The mass loss of rotating stars is of necessity anisotropic, with a fast wind emerging from the hotter polar caps, while an ejection of an equatorial ring may occur if the opacity in these regions grows rapidly for decreasing effective temperature. The mass loss may reach large values if a star reaches the rotationally-modified Eddington limit, the so-called $\Omega\Gamma$ -limit (Maeder & Meynet 2000). The effect is assumed to play an important role in the ejection of LBV nebulae (Lamers et al. 2001). After our revision of its mass, Sher 25 is clearly unrelated to LBVs: it is significantly less luminous than the classical LBVs and much hotter than the low-luminosity LBVs. Can the $\Omega\Gamma$ -limit have played a role in the formation of the hourglass nebula? Combining our $v \sin i$ of 60 km s^{-1} with the inclination angle of 64° derived by Brandner et al. (1997b) by assuming an intrinsic circular ring geometry (in the star's equatorial plane), one finds a rotational velocity of 67 km s^{-1} for Sher 25. This is about three times higher than the rotational velocity implied by an (interpolated) $27 M_{\odot}$ Geneva model with an initial $\Omega_{\text{rot}} = 0.568 \Omega_{\text{crit}}$ for the parameters of Sher 25. Near the TAMS the rotational velocity for the star, which was more compact at that time, would have been about twice as large, still very far away from critical rotation – more-

over, Sher 25 is far from the Eddington limit. Consequently, the star was never close to the $\Omega\Gamma$ -limit (note that two of our sample stars show a similar $v \sin i$, so Sher 25 is not unusual in this regard).

Alternatively, bipolar outflows including hourglass nebulae are often found for planetary nebulae, considered to be formed during the common-envelope phase in a binary system (e.g. Ondratschek et al. 2022, and references therein). Such a scenario was also invoked to produce the triple ring nebula around the precursor of SN 1987A (Podsiadlowski 1992; Morris & Podsiadlowski 2007). In order to reproduce the dynamics of the hourglass nebula around Sher 25 and the total ejected mass of 0.3 to $0.6 M_{\odot}$ (Brandner et al. 1997a) and the offset of the equatorial ring from the central star (Brandner et al. 1997b), Morris & Podsiadlowski (2009) suggested that a binary merger had occurred during the Hertzsprung crossing when the envelope had a radius $\sim 300 R_{\odot}$, that is before the RSG phase, as indicated by the CNO mixing signature. The occurrence of the merger and not orbital shrinkage was backed by Taylor et al. (2014), who found Sher 25 to be a single star. They attributed some small-scale radial velocity variations to pulsations. Sher 25 may still be in a thermal readjustment phase after the merger and nebula ejection some 6600 yr ago. Consequently, only our atmospheric parameters, the luminosity and radius may be firm, whereas the mass and age – which were derived by considering (single star) evolution models – need to be treated with caution. However, it still may be safe to assume Sher 25 to be significantly older than NGC 3603, while its mass may be even lower than inferred in the single-star scenario.

We conclude that our work finds Sher 25 to be much closer in properties to Sk-69°202, the precursor of SN 1987A, than previously assumed. It is therefore also more similar to the other two B1 supergiants with bipolar nebulae, [SBW2007] 1 (Smith et al. 2007) and MN18 (Gvaramadze et al. 2015), and the cooler analogues HD 168625 (B6 Iap, Smith 2007) and HD 93795 (B9 Ia, Gvaramadze et al. 2020), at similar luminosities.

Acknowledgements. D.W., A.E. and N.P. gratefully acknowledge support from the Austrian Science Fund FWF project DK-ALM, grant W1259-N27. We thank M. Urbaneja and S. Kimeswenger for valuable discussions. We are grateful to A. Irrgang for several updates of DETAIL and SURFACE. We want to thank the referee for valuable suggestions to improve the paper. Based on observations collected at the European Southern Observatory under ESO programmes 075.D-0103(A) – PI Dufton, 082.D-0136(A) – PI Evans, 091.D-0221(A) – PI Przybilla, obtained from the ESO Science Archive Facility with DOI: <https://doi.org/10.18727/archive/24>, and on programme 381.D-0914(A) – PI Rochau, with DOI: <https://doi.org/10.18727/archive/27>. Based on observations collected at the Centro Astronómico Hispano Alemán at Calar Alto (CAHA), operated jointly by the Max-Planck Institut für Astronomie and the Instituto de Astrofísica de Andalucía (CSIC), proposal H2005-2.2-016. The latter observational data are available under <https://doi.org/10.5281/zenodo.8230158>. This research used the facilities of the Canadian Astronomy Data Centre operated by the National Research Council of Canada with the support of the Canadian Space Agency. This work has made use of data from the European Space Agency (ESA) mission *Gaia* (<https://www.cosmos.esa.int/gaia>), processed by the *Gaia* Data Processing and Analysis Consortium (DPAC, <https://www.cosmos.esa.int/web/gaia/dpac/consortium>). Funding for the DPAC has been provided by national institutions, in particular the institutions participating in the *Gaia* Multilateral Agreement. This publication makes use of data products from the Two Micron All Sky Survey, which is a joint project of the University of Massachusetts and the Infrared Processing and Analysis Center/California Institute of Technology, funded by the National Aeronautics and Space Administration and the National Science Foundation. This publication makes use of data products from the Wide-field Infrared Survey Explorer, which is a joint project of the University of California, Los Angeles, and the Jet Propulsion Laboratory/California Institute of Technology, funded by the National Aeronautics and Space Administration. This research has made use of the SVO Filter Profile Service (<http://svo2.cab.inta-csic.es/theory/fps/>) supported from the Spanish MINECO through grant AYA2017-84089.

References

- Abt, H. A. & Levy, S. G. 1973, *ApJ*, 184, 167
- Aerts, C., Bowman, D. M., Simon-Díaz, S., et al. 2018, *MNRAS*, 476, 1234
- Allan, C. & Santillan, A. 1991, *Rev. Mexicana Astron. Astrofis.*, 22, 255
- Arellano-Córdova, K. Z., Esteban, C., García-Rojas, J., & Méndez-Delgado, J. E. 2020, *MNRAS*, 496, 1051
- Aschenbrenner, P., Przybilla, N., & Butler, K. 2023, *A&A*, 671, A36
- Baier, G., Ladebeck, R., & Weigelt, G. 1985, *A&A*, 151, 61
- Bailer-Jones, C. A. L., Rybizki, J., Fousneau, M., Demleitner, M., & Andrae, R. 2021, *AJ*, 161, 147
- Bragança, G. A., Daflon, S., Lanz, T., et al. 2019, *A&A*, 625, A120
- Brandner, W., Chu, Y.-H., Eisenhauer, F., Grebel, E. K., & Points, S. D. 1997a, *ApJ*, 489, L153
- Brandner, W., Grebel, E. K., Chu, Y.-H., & Weis, K. 1997b, *ApJ*, 475, L45
- Burrows, C. J., Krist, J., Hester, J. J., et al. 1995, *ApJ*, 452, 680
- Butler, K. & Giddings, J. R. 1985, *Newsletter of Analysis of Astronomical Spectra*, 9 (Univ. London)
- Chini, R., Hoffmeister, V. H., Nasser, A., Stahl, O., & Zinnecker, H. 2012, *MNRAS*, 424, 1925
- Chita, S. M., Langer, N., van Marle, A. J., García-Segura, G., & Heger, A. 2008, *A&A*, 488, L37
- Crowther, P. A., Lennon, D. J., & Walborn, N. R. 2006, *A&A*, 446, 279
- Currie, T., Hernandez, J., Irwin, J., et al. 2010, *ApJS*, 186, 191
- Cutri, R. M., Skrutskie, M. F., van Dyk, S., et al. 2003, *VizieR Online Data Catalog*, II/246
- Cutri, R. M., Wright, E. L., Conrow, T., et al. 2021, *VizieR Online Data Catalog*, II/328
- da Silva, R., Lemasle, B., Bono, G., et al. 2016, *A&A*, 586, A125
- de Burgos, A., Simon-Díaz, S., Lennon, D. J., et al. 2020, *A&A*, 643, A116
- de Vegt, C. & Gehlich, U. K. 1976, *A&A*, 48, 245
- Dufton, P. L., Ryans, R. S. I., Trundle, C., et al. 2005, *A&A*, 434, 1125
- Eggenberger, P., Ekström, S., Georgy, C., et al. 2021, *A&A*, 652, A137
- Ekström, S., Georgy, C., Eggenberger, P., et al. 2012, *A&A*, 537, A146
- Evans, D. S. & Edwards, D. A. 1981, *AJ*, 86, 1277
- Firnstein, M. & Przybilla, N. 2012, *A&A*, 543, A80
- Fitzpatrick, E. L. 1999, *PASP*, 111, 63
- Fousneau, M., Frémat, Y., Andrae, R., et al. 2023, *A&A*, 674, A28
- Fraser, M., Dufton, P. L., Hunter, I., & Ryans, R. S. I. 2010, *MNRAS*, 404, 1306
- Gaia Collaboration. 2022, *VizieR Online Data Catalog*, I/355
- Gaia Collaboration, Brown, A. G. A., Vallenari, A., et al. 2021, *A&A*, 649, A1
- Gaia Collaboration, Prusti, T., de Bruijne, J. H. J., et al. 2016, *A&A*, 595, A1
- Georgy, C., Ekström, S., Eggenberger, P., et al. 2013, *A&A*, 558, A103
- Giddings, J. R. 1981, PhD thesis, (Univ. London)
- Gontcharov, G. A. 2006, *Astronomy Letters*, 32, 759
- González, J. F., Briquet, M., Przybilla, N., et al. 2019, *A&A*, 626, A94
- González, J. F., Hubrig, S., Przybilla, N., et al. 2017, *MNRAS*, 467, 437
- Gravity Collaboration, Abuter, R., Amorim, A., et al. 2019, *A&A*, 625, L10
- Gray, R. O. & Corbally, C. J. 2009, *Stellar Spectral Classification* (Princeton: Princeton University Press)
- Gvaramadze, V. V., Kniazev, A. Y., Bestenlehner, J. M., et al. 2015, *MNRAS*, 454, 219
- Gvaramadze, V. V., Kniazev, A. Y., Castro, N., & Katkov, I. Y. 2020, *MNRAS*, 492, 2383
- Harayama, Y., Eisenhauer, F., & Martins, F. 2008, *ApJ*, 675, 1319
- Hendry, M. A., Smartt, S. J., Skillman, E. D., et al. 2008, *MNRAS*, 388, 1127
- Hillier, D. J. & Miller, D. L. 1998, *ApJ*, 496, 407
- Hirsch, H. A. 2009, PhD thesis, (Univ. Erlangen-Nürnberg)
- Houk, N., Hartoog, M. R., & Cowley, A. P. 1976, *AJ*, 81, 116
- Hubeny, I. 1988, *Comput. Phys. Commun.*, 52, 103
- Hubeny, I. & Lanz, T. 1995, *ApJ*, 439, 875
- Humphreys, R. M. & Davidson, K. 1979, *ApJ*, 232, 409
- Irgang, A., Przybilla, N., Heber, U., et al. 2014, *A&A*, 565, A63
- Irgang, A., Przybilla, N., & Meynet, G. 2022, *Nat. Astron.*, 6, 1414
- Kaufer, A., Stahl, O., Tubbesing, S., et al. 1999, *The Messenger*, 95, 8
- Kuhn, M. A., Medina, N., Getman, K. V., et al. 2017, *AJ*, 154, 87
- Kurucz, R. 1993, CD-ROM No. 13 (Cambridge, Mass.: SAO)
- Lamers, H. J. G. L. M., Nota, A., Panagia, N., Smith, L. J., & Langer, N. 2001, *ApJ*, 551, 764
- Langer, N. 2012, *ARA&A*, 50, 107
- Langer, N. & Kudritzki, R. P. 2014, *A&A*, 564, A52
- Lennon, D. J., Dufton, P. L., & Fitzsimmons, A. 1992, *A&AS*, 94, 569
- Levato, H., Morrell, N., Garcia, B., & Malaroda, S. 1988, *ApJS*, 68, 319
- Maeder, A. & Meynet, G. 2000, *A&A*, 361, 159
- Maeder, A. & Meynet, G. 2012, *Rev. Mod. Phys.*, 84, 25
- Maeder, A., Przybilla, N., Nieva, M. F., et al. 2014, *A&A*, 565, A39
- Maíz Apellániz, J., Barbá, R. H., Fernández Aranda, R., et al. 2022, *A&A*, 657, A131
- Maíz Apellániz, J., Crespo Bellido, P., Barbá, R. H., Fernández Aranda, R., & Sota, A. 2020, *A&A*, 643, A138
- Manset, N. & Donati, J.-F. 2003, *Proc. SPIE*, 4843, 425
- Markova, N. & Puls, J. 2008, *A&A*, 478, 823
- Melena, N. W., Massey, P., Morrell, N. I., & Zangari, A. M. 2008, *AJ*, 135, 878
- Mermilliod, J. C. 1997, *VizieR Online Data Catalog*, 2168
- Montegriffo, P., De Angeli, F., Andrae, R., et al. 2023, *A&A*, 674, A3
- Morel, T. & Butler, K. 2008, *A&A*, 487, 307
- Morel, T., Butler, K., Aerts, C., Neiner, C., & Briquet, M. 2006, *A&A*, 457, 651
- Morris, T. & Podsiadlowski, P. 2007, *Science*, 315, 1103
- Morris, T. & Podsiadlowski, P. 2009, *MNRAS*, 399, 515
- Najarro, F., Hillier, D. J., Puls, J., Lanz, T., & Martins, F. 2006, *A&A*, 456, 659
- Nieva, M. F. & Przybilla, N. 2006, *ApJ*, 639, L39
- Nieva, M. F. & Przybilla, N. 2007, *A&A*, 467, 295
- Nieva, M. F. & Przybilla, N. 2008, *A&A*, 481, 199
- Nieva, M. F. & Przybilla, N. 2012, *A&A*, 539, A143
- Nieva, M. F. & Przybilla, N. 2014, *A&A*, 566, A7
- Nieva, M. F. & Simón-Díaz, S. 2011, *A&A*, 532, A2
- Odenkirchen, M. & Brosche, P. 1992, *Astronomische Nachrichten*, 313, 69
- Ondratschek, P. A., Röpké, F. K., Schneider, F. R. N., et al. 2022, *A&A*, 660, L8
- Pang, X., Pasquali, A., & Grebel, E. K. 2011, *AJ*, 142, 132
- Pasquini, L., Avila, G., Blecha, A., et al. 2002, *The Messenger*, 110, 1
- Pavlovski, K., Southworth, J., Tkachenko, A., Van Reeth, T., & Tamajo, E. 2023, *A&A*, 671, A139
- Pfeiffer, M. J., Frank, C., Baumüller, D., Fuhrmann, K., & Gehren, T. 1998, *A&AS*, 130, 381
- Podsiadlowski, P. 1992, *PASP*, 104, 717
- Przybilla, N. 2005, *A&A*, 443, 293
- Przybilla, N. & Butler, K. 2001, *A&A*, 379, 955
- Przybilla, N. & Butler, K. 2004, *ApJ*, 609, 1181
- Przybilla, N., Butler, K., Becker, S. R., & Kudritzki, R. P. 2001, *A&A*, 369, 1009
- Przybilla, N., Butler, K., Becker, S. R., & Kudritzki, R. P. 2006, *A&A*, 445, 1099
- Przybilla, N., Butler, K., Becker, S. R., Kudritzki, R. P., & Venn, K. A. 2000, *A&A*, 359, 1085
- Przybilla, N., Firnstein, M., Nieva, M. F., Meynet, G., & Maeder, A. 2010, *A&A*, 517, A38
- Przybilla, N., Nieva, M. F., & Butler, K. 2008, *ApJ*, 688, L103
- Przybilla, N., Nieva, M. F., Irgang, A., & Butler, K. 2013, *EAS Publ. Ser.*, 63, 13
- Puls, J., Urbaneja, M. A., Venero, R., et al. 2005, *A&A*, 435, 669
- Radick, R. R., Africano, J. L., Flores, M. R., Klimke, D. A., & Tyson, E. T. 1982, *AJ*, 87, 1874
- Rodrigo, C. & Solano, E. 2020, in *Contributions to the XIV.0 Scientific Meeting (virtual) of the Spanish Astronomical Society*, 182
- Rodrigo, C., Solano, E., & Bayo, A. 2012, *SVO Filter Profile Service Version 1.0*, IVOA Working Draft 15 October 2012
- Roman-Lopes, A., Franco, G. A. P., & Sanmartín, D. 2016, *ApJ*, 823, 96
- Santolaya-Rey, A. E., Puls, J., & Herrero, A. 1997, *A&A*, 323, 488
- Schiller, F. & Przybilla, N. 2008, *A&A*, 479, 849
- Searle, S. C., Prinja, R. K., Massa, D., & Ryans, R. 2008, *A&A*, 481, 777
- Sher, D. 1965, *MNRAS*, 129, 237
- Simón-Díaz, S., Godart, M., Castro, N., et al. 2017, *A&A*, 597, A22
- Skillman, E. D. 1998, in *Stellar astrophysics for the local group: VIII Canary Islands Winter School of Astrophysics*, ed. A. Aparicio, A. Herrero, & F. Sánchez, 457
- Smartt, S. J., Lennon, D. J., Kudritzki, R. P., et al. 2002, *A&A*, 391, 979
- Smith, N. 2007, *AJ*, 133, 1034
- Smith, N., Bally, J., & Walawender, J. 2007, *AJ*, 134, 846
- Sung, H. & Bessell, M. S. 2004a, *AJ*, 127, 1014
- Sung, H. & Bessell, M. S. 2004b, *AJ*, 127, 1014
- Sung, H., Sana, H., & Bessell, M. S. 2013, *AJ*, 145, 37
- Taylor, W. D., Evans, C. J., Simón-Díaz, S., et al. 2014, *MNRAS*, 442, 1483
- Thompson, G. I., Nandy, K., Jamar, C., et al. 1995, *VizieR Online Data Catalog*, II/59B
- Tokovinin, A., Mason, B. D., & Hartkopf, W. I. 2010, *AJ*, 139, 743
- van Leeuwen, F. 2007, *A&A*, 474, 653
- Vrancken, M., Butler, K., & Becker, S. R. 1996, *A&A*, 311, 661
- Walborn, N. R., Prevot, M. L., Prevot, L., et al. 1989, *A&A*, 219, 229
- Wampler, E. J., Wang, L., Baade, D., et al. 1990, *ApJ*, 362, L13
- Weis, K. 2011, in *Active OB Stars: Structure, Evolution, Mass Loss, and Critical Limits*, ed. C. Neiner, G. Wade, G. Meynet, & G. Peters, Vol. 272, 372–377
- Wesseliüs, P. R., van Duinen, R. J., de Jonge, A. R. W., et al. 1982, *A&AS*, 49, 427
- Weßmayer, D., Przybilla, N., & Butler, K. 2022, *A&A*, 668, A92
- Yershov, V. N. 2014, *Ap&SS*, 354, 97
- Yusof, N., Hirschi, R., Eggenberger, P., et al. 2022, *MNRAS*, 511, 2814

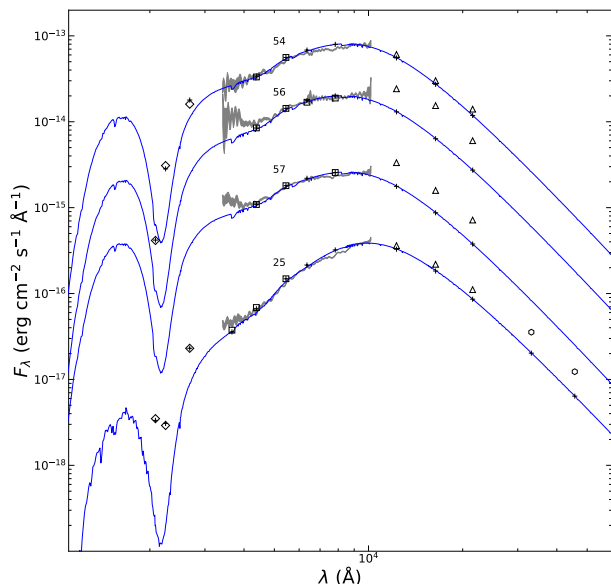


Fig. A.1. Comparison of stellar model SEDs and photometry for a subset of the cluster members depicted in Fig. 11. Symbol assignment is analogous to Fig. 10. Johnson-Cousins R_c & I_c are shown as black squares. For better visibility, the SEDs were shifted by +1 dex for NGC 3603 54, -1 dex for NGC 3603 57, and -2.5 dex for Sher 25.

Appendix A: IR excess in NGC 3603

Sher 25 shows a notable observational IR excess, present already in the 2MASS J , H , and K filters, as well as the WISE bands. While some excess flux in W2 is also present in most comparison stars, this behaviour is unusual for J , H , K , and W1 (see the discussion in Sect. 4.6). As can be seen in Fig. A.1, a similar excess is also observed for some bona-fide cluster members of NGC 3603 (see discussion in Sect. 6). For a useful comparison, model stellar spectra – corresponding to spectral type O3 V for NGC 3603 56 and 57, and O6 V for NGC 3603 54 – were downloaded from the Castelli-Kurucz atlas¹⁰. For NGC 3603 56 and 57, which are located in a region with stronger background glow, it is apparent that an accurate fitting of the UV and optical photometry precludes a reproduction of the IR data without assumption of an extra component. A very mild excess is present in NGC 3603 54, likely due to its location in a region with almost absent background glow.

Appendix B: The Gaia DR3 distance to NGC 3603

The sight line towards NGC 3603 is complicated for distance determinations because it traverses the Carina spiral arm – one of the most active regions of massive star formation in the Milky Way – close to tangentially over a large region. Chance projections of foreground or background early-type stars on the cluster area can therefore be expected.

A comprehensive overview of distances to NGC 3603 from the literature that predated parallax measurements by the Gaia mission is given in Table A.1 of Maíz Apellániz et al. (2020). Most values from the 18 studies lie in the range 6.0 to 8.5 kpc, with some outliers. Maíz Apellániz et al. (2020) themselves derived a Gaia DR2-based distance of 8000^{+2600}_{-1700} pc, which was recently updated to a value of 7130^{+590}_{-500} pc (Maíz Apellániz et al.

¹⁰ <https://www.stsci.edu/hst/instrumentation/reference-data-for-calibration-and-tools/astronomical-catalogs/castelli-and-kurucz-atlas>

2022) based on Gaia EDR3 data. A total of 166 stars contributed to the latter value after filtering an initial number of about 28 600 stars in the area of NGC 3603 within a circle centred on right ascension $\alpha = 168^{\circ}79$ and declination $\delta = -61^{\circ}26$ with a radius of $206''$ according to the Renormalised Unit Weight Error (RUWE), position, proper motion and colour.

As the uncertainties in the cluster distance are substantial – note that active massive star formation in the wider area of NGC 3603 is ongoing (Roman-Lopes et al. 2016) with a possible substantial extension also in distance – we tried a modified approach to improve on the cluster distance. We concentrated on the inner cluster ($1' \times 1'$ field) as investigated by Melena et al. (2008), employing only stars with Gaia EDR3 parallaxes and known (early) spectral type (from Table 3 of Melena et al. 2008). The resulting star sample is summarised in Table B.1, which contains the star name, as resolved by SIMBAD¹¹, the spectral type, Gaia EDR3 parallax ϖ and proper motion components in right ascension μ_α and declination μ_δ , the Gaia G magnitude, the RUWE and the photogeometric distance (Bailer-Jones et al. 2021). The latter values and the parallaxes show that Gaia measurements considering solely the first 34 months of the mission are strongly limited in accuracy and precision for such distant stars. From this star sample, further objects were removed for RUWE values >1.3 , which is an indication of possible binarity, or because of discrepant proper motions, as visualised in Fig. B.1. The remaining stars are marked in boldface style in Table B.1 for which a histogram of the distance distribution is also shown in Fig. B.1. We note that the two late-O and early-B supergiants NGC 3603 23 and 25, aka Sher 23 (OC9.7 Ia) and our sample star Sher 25 were also removed because they do not match the 1 to 2 Myr isochrone of NGC 3603 (Fig. 7 of Melena et al. 2008), but instead appear to be significantly older. We also note that we do not expect crowding effects on the parallaxes, as all selected stars are isolated (cf. Fig. 1 and 2 of Melena et al., and our Fig. 1) and separated by $>8''$ from the cluster centre.

The distance to NGC 3603 was consequently calculated from the remaining 10 stars to $d_{\text{NGC3603}} = 6250$ pc with a standard error of 150 pc and a 1σ standard deviation of 460 pc. This is somewhat shorter than the 7130^{+590}_{-500} pc value of Maíz Apellániz et al. (2022) but compatible within the mutual uncertainties. A significant reduction of the uncertainties has to await further Gaia data releases based on a longer measurement period and a better understanding of systematic effects.

Finally, we want to comment on the atmospheric parameters that were provided in the full Gaia DR3 (Gaia Collaboration 2022). Effective temperatures, surface gravities and metallicities are found for ten out of the 23 stars from Table B.1. All these confuse the O-stars and Sher 25 with metal-poor giants with $T_{\text{eff}} < 10\,000$ K (with one exception at $\sim 17\,000$ K). Apparently, the Gaia astrophysical parameters inference system (Apsis, Fouesneau et al. 2023) needs to be improved in order to enable it to correctly characterise significantly reddened O-type stars, similar to the case of mildly-reddened late O-type stars (Aschenbrenner et al. 2023).

Appendix C: Global model fit for Sher 25

A comparison of the observed FEROS spectrum of Sher 25 with the best fitting global synthetic spectrum is shown in the following Figs. C.1 to C.9. The model was computed with the ARLAS9/DETAIL/SURFACE codes based on atmospheric parameters and

¹¹ <http://simbad.u-strasbg.fr/simbad/sim-fid>

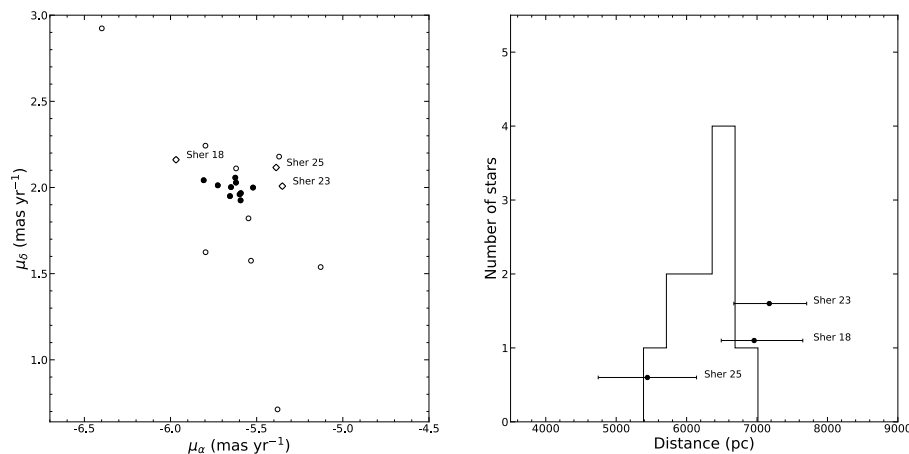


Fig. B.1. Gaia EDR3 proper motions (Gaia Collaboration et al. 2021) and photogeometric distances (Bailer-Jones et al. 2021) of presumed member stars of NGC 3603 identified in Table B.1. *Left panel:* proper motions in right ascension μ_α and in declination μ_δ . Objects depicted as full symbols satisfy our selection criteria, while those marked by empty symbols are excluded for high RUWE values >1.3 or constraints in proper motion. *Right panel:* distribution of inferred distances towards NGC 3603. The BSGs in the inner NGC 3603 field (Sher 25, Sher 23, and Sher 18) are marked in both panels.

Table B.1. Gaia EDR3 parallaxes and photometric and astrometric measurements for stars in NGC 3603.

Name	Sp. Type ^d	ϖ (mas)	μ_α (mas yr ⁻¹)	μ_δ (mas yr ⁻¹)	G (mag)	RUWE	d (pc) ^b
NGC 3603 18	O3.5 If	0.1428 ± 0.0111	-5.968 ± 0.012	2.161 ± 0.011	11.9722	0.99	6960^{+690}_{-470}
NGC 3603 19	O3 V((f))	0.0897 ± 0.0114	-5.370 ± 0.012	2.179 ± 0.012	13.1764	1.02	7780^{+850}_{-630}
NGC 3603 21	O6 V((f))	0.1147 ± 0.0160	-5.593 ± 0.019	1.925 ± 0.017	14.2138	1.00	6400^{+790}_{-500}
NGC 3603 22	O3 III(f)	0.1430 ± 0.0170	-5.808 ± 0.018	2.042 ± 0.018	12.7677	1.07	6470^{+770}_{-640}
NGC 3603 23	OC9.7 Ia	0.1344 ± 0.0112	-5.351 ± 0.012	2.008 ± 0.011	12.1323	0.98	7170^{+530}_{-500}
NGC 3603 24	O6 V	0.1161 ± 0.0152	-5.592 ± 0.016	1.967 ± 0.015	13.7393	1.13	6130^{+570}_{-490}
NGC 3603 25	B1 Iab	0.1560 ± 0.0166	-5.387 ± 0.020	2.116 ± 0.015	11.4261	0.94	5740^{+800}_{-420}
NGC 3603 27	O7.5 V	0.1321 ± 0.0182	-5.599 ± 0.022	1.960 ± 0.022	14.5238	1.03	5390^{+600}_{-330}
NGC 3603 47	O4 V	0.1248 ± 0.0103	-5.797 ± 0.011	2.243 ± 0.010	12.1486	0.94	7910^{+580}_{-510}
NGC 3603 49	O7.5 V	0.1845 ± 0.0588	-5.129 ± 0.065	1.538 ± 0.060	14.1456	4.01	3830^{+930}_{-430}
NGC 3603 53	O8.5 V	0.2227 ± 0.0466	-5.619 ± 0.053	2.111 ± 0.040	13.9243	3.25	3330^{+830}_{-340}
NGC 3603 54	O6 V	0.1139 ± 0.0147	-5.655 ± 0.016	1.950 ± 0.015	14.0344	0.97	6360^{+490}_{-420}
NGC 3603 56	O3 III(f)	0.1254 ± 0.0216	-5.620 ± 0.022	2.028 ± 0.022	12.9838	1.04	6660^{+1010}_{-460}
NGC 3603 57	O3 III(f)	0.1521 ± 0.0119	-5.649 ± 0.013	2.002 ± 0.013	12.7444	1.01	6390^{+470}_{-430}
NGC 3603 63	O3.5 III(f)	0.0053 ± 0.0407	-5.533 ± 0.055	1.575 ± 0.037	12.9097	1.91	9300^{+1640}_{-1090}
NGC 3603 64	O3 V((f))	0.1097 ± 0.0127	-5.521 ± 0.014	2.000 ± 0.012	13.0839	1.15	7010^{+650}_{-480}
CI* NGC 3603 MMM 102	O8.5 V	0.1178 ± 0.0602	-5.379 ± 0.066	0.712 ± 0.062	14.8683	2.57	4450^{+710}_{-540}
CI* NGC 3603 MMM 103	O3 V((f))	0.1583 ± 0.0159	-5.624 ± 0.016	2.057 ± 0.027	12.6349	0.97	5950^{+550}_{-440}
CI* NGC 3603 MMM 104	O3 III(f)	0.0617 ± 0.0442	-5.548 ± 0.065	1.821 ± 0.037	12.5400	2.42	7200^{+1110}_{-1010}
CI* NGC 3603 MMM 108	O5.5 V	-0.1445 ± 0.1030	-5.797 ± 0.111	1.624 ± 0.113	13.2060	5.83	5200^{+2890}_{-1080}
CI* NGC 3603 MMM 117	O6 V	0.1043 ± 0.0275	-5.726 ± 0.042	2.012 ± 0.025	13.6948	1.28	5790^{+650}_{-560}
CI* NGC 3603 BLW A2	O3 V	1.1375 ± 0.4312	-8.387 ± 0.420	1.162 ± 0.419	10.5626	13.59	750^{+1450}_{-110}
CI* NGC 3603 BLW A3	O3 III(f*)	0.5897 ± 0.1579	-6.399 ± 0.174	2.923 ± 0.438	10.7691	4.22	1420^{+300}_{-180}

Notes. The objects used for the distance estimate of NGC 3603 are set in boldface style. We rejected the other objects based on their RUWE factor or discrepant proper motions. The supergiants NGC 3603 23 and NGC 3603 25 (i. e. Sher 25) were rejected because their ages are incompatible with the cluster isochrone of 1 to 2 Myr (Melena et al. 2008). Star identifications for the first 16 objects are from Sher (1965), for the following five objects from Melena et al. (2008) and for the final two objects from Baier et al. (1985). ^(a) From Table 3 of Melena et al. (2008) except for NGC 3603 56, for which the spectral type of the primary component from their Table 1 is given. ^(b) Photogeometric distances (Bailer-Jones et al. 2021).

elemental abundances as summarised in Tables 3 and 4, respectively. With the exception of N III $\lambda\lambda 4634$ and 4640 \AA , all visible spectral lines of stellar origin are accounted for by the synthetic model spectrum. The diagnostic stellar lines are identified. We note that the lower Balmer lines, in particular $H\alpha$ and $H\beta$, but also $H\gamma$ to a lesser degree, as well as the strong red He I $\lambda 5785$, 6678 and 7065 \AA lines are affected by the stellar wind, which is unaccounted for by the hydrostatic model. We also want to mention the difficulties in reproducing the C II $\lambda\lambda 4267$ and $6578/82 \text{ \AA}$ lines closely, as addressed in Sect. 4.3. Multiple interstellar ('IS') atomic lines, such as the Ca II H and K lines, the Ca I $\lambda 4226 \text{ \AA}$,

the Na D lines, the K I $\lambda\lambda 7664.9$ and 7698.9 \AA (the former partially overlaps with a telluric line of O₂) and also molecular absorption lines of CH $\lambda 4300$ as well as CH⁺ $\lambda\lambda 3957$ and 4232 \AA , are also identified. Note that they are blue-shifted in the observed spectrum because the stellar features were corrected to the laboratory rest frame. In addition, we emphasise the presence of numerous diffuse interstellar bands (DIBs) of considerable strength, mediated by the high reddening along the sight line towards Sher 25. These are absent in the model, as well as the numerous sharp telluric water vapour features and the A-, B- and γ -bands of O₂ towards the red part of the spectrum.

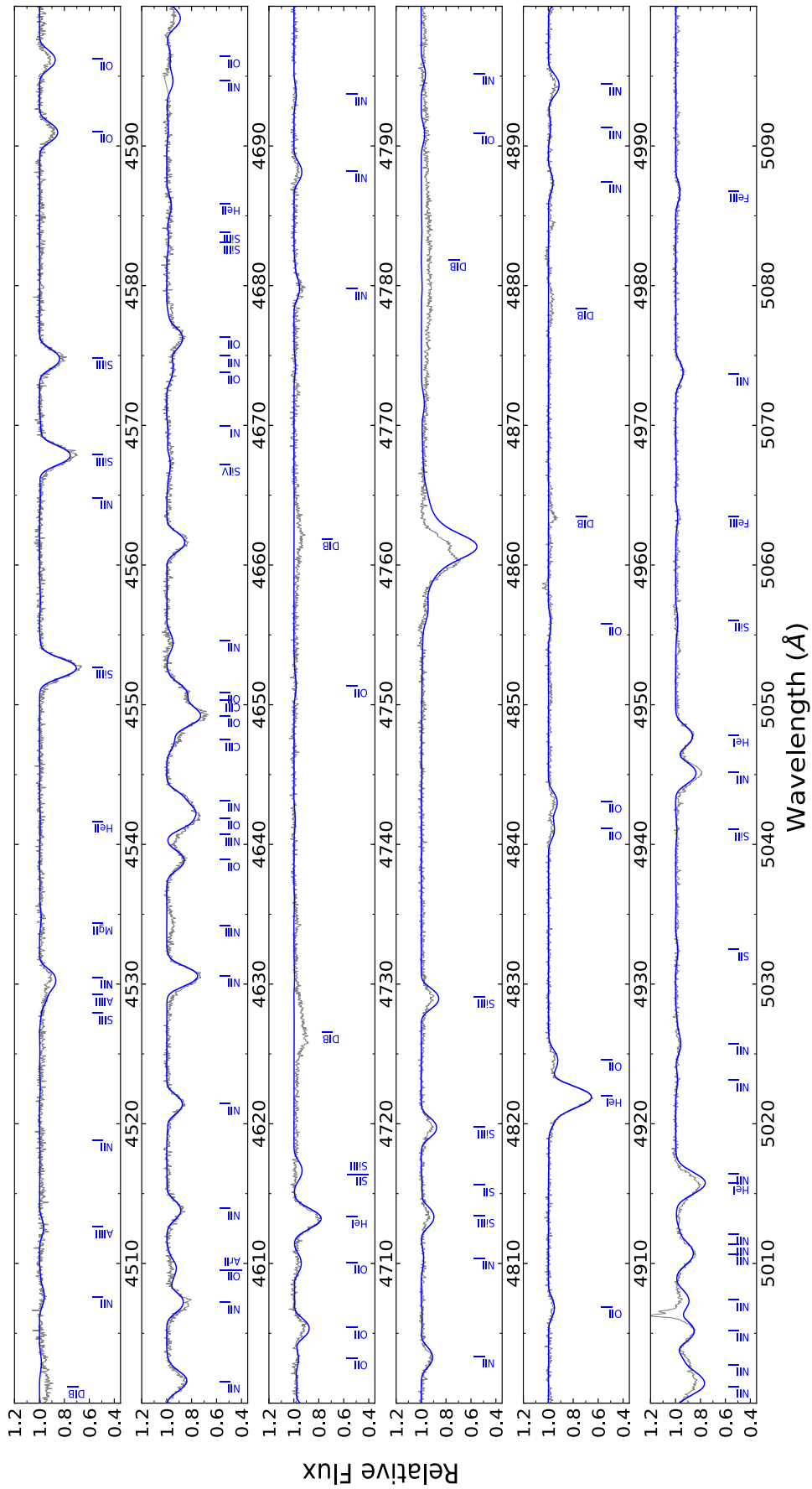


Fig. C.2. Same as Fig. C.1, but in the wavelength range $\lambda\lambda 4500\text{--}5100\text{ \AA}$.

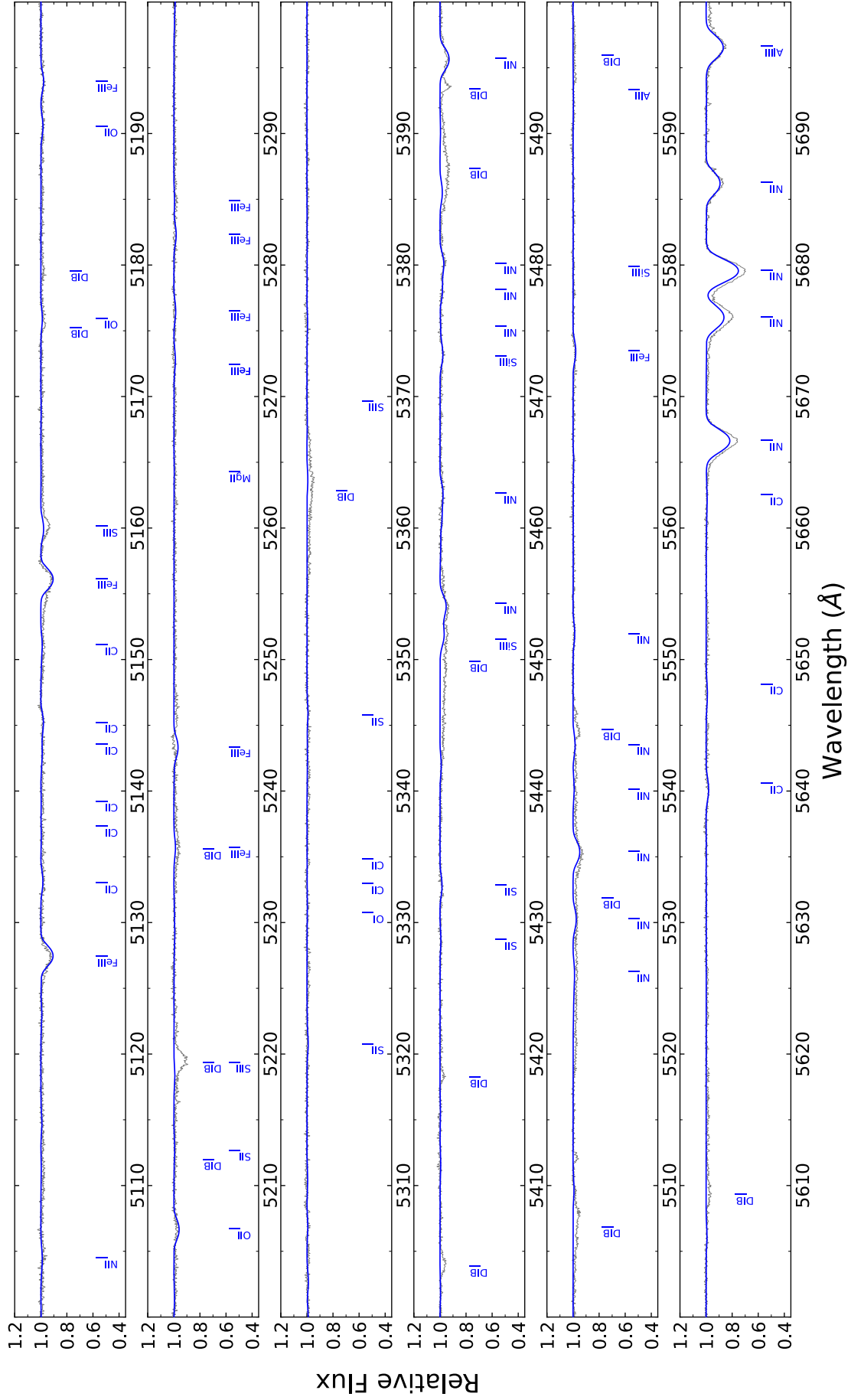


Fig. C.3. Same as Fig. C.1, but in the wavelength range $\lambda\lambda 5100\text{--}5700$ Å.

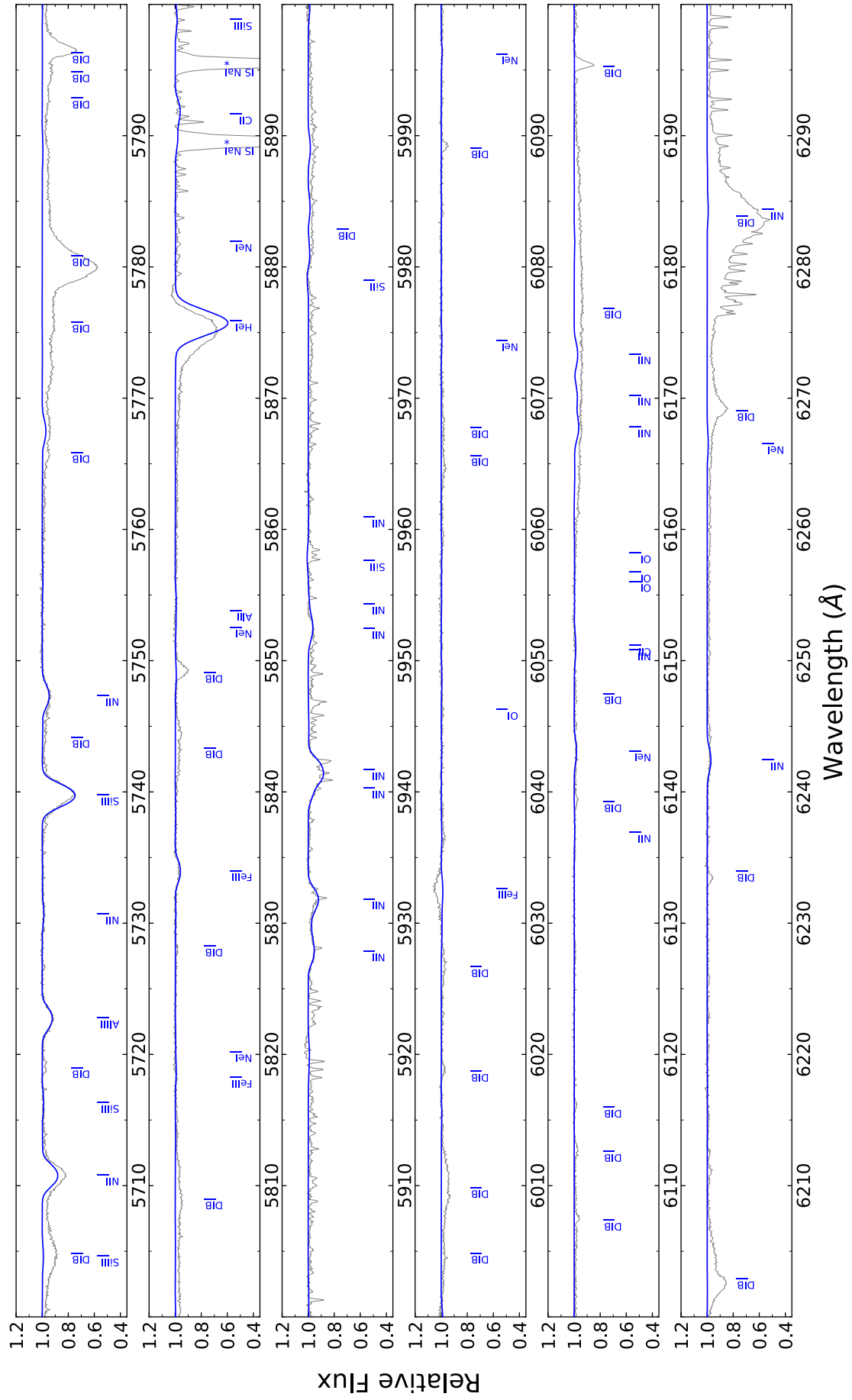


Fig. C.4. Same as Fig. C.1, but in the wavelength range $\lambda\lambda 5700\text{--}6300\text{ \AA}$.

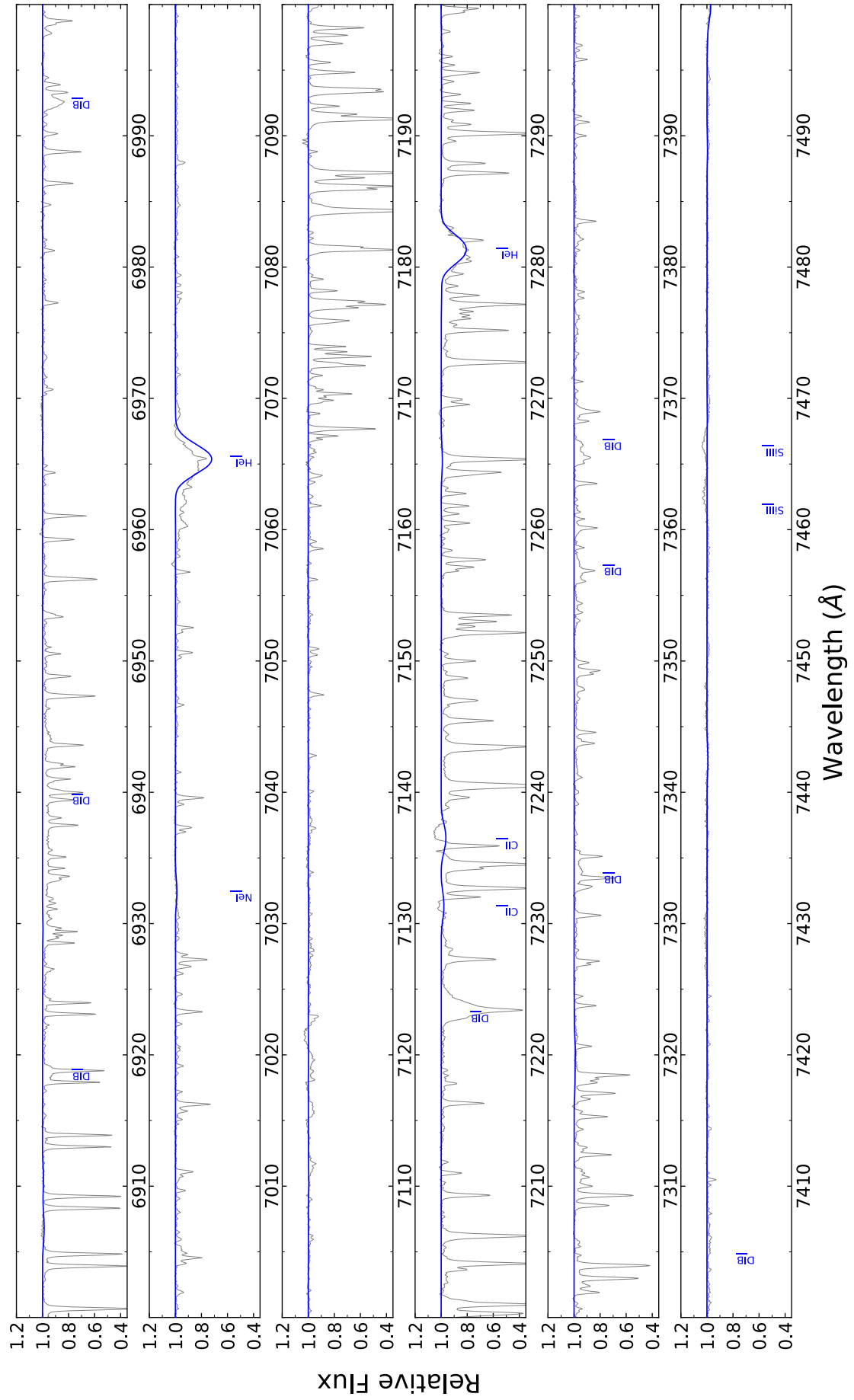


Fig. C.6. Same as Fig. C.1, but in the wavelength range $\lambda\lambda 6900\text{--}7500$ Å.

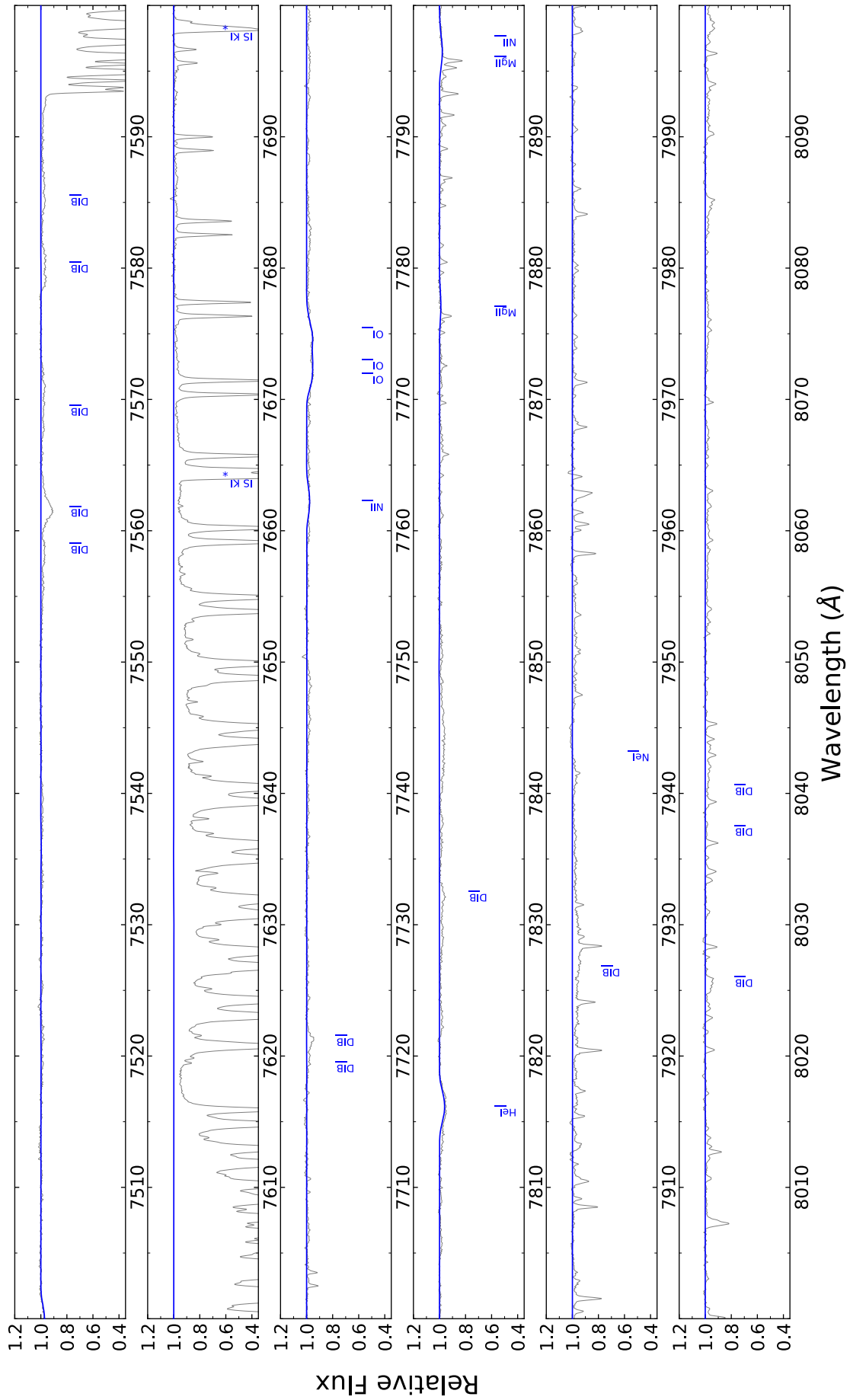


Fig. C.7. Same as Fig. C.1, but in the wavelength range $\lambda\lambda 7500\text{--}8100 \text{ \AA}$.

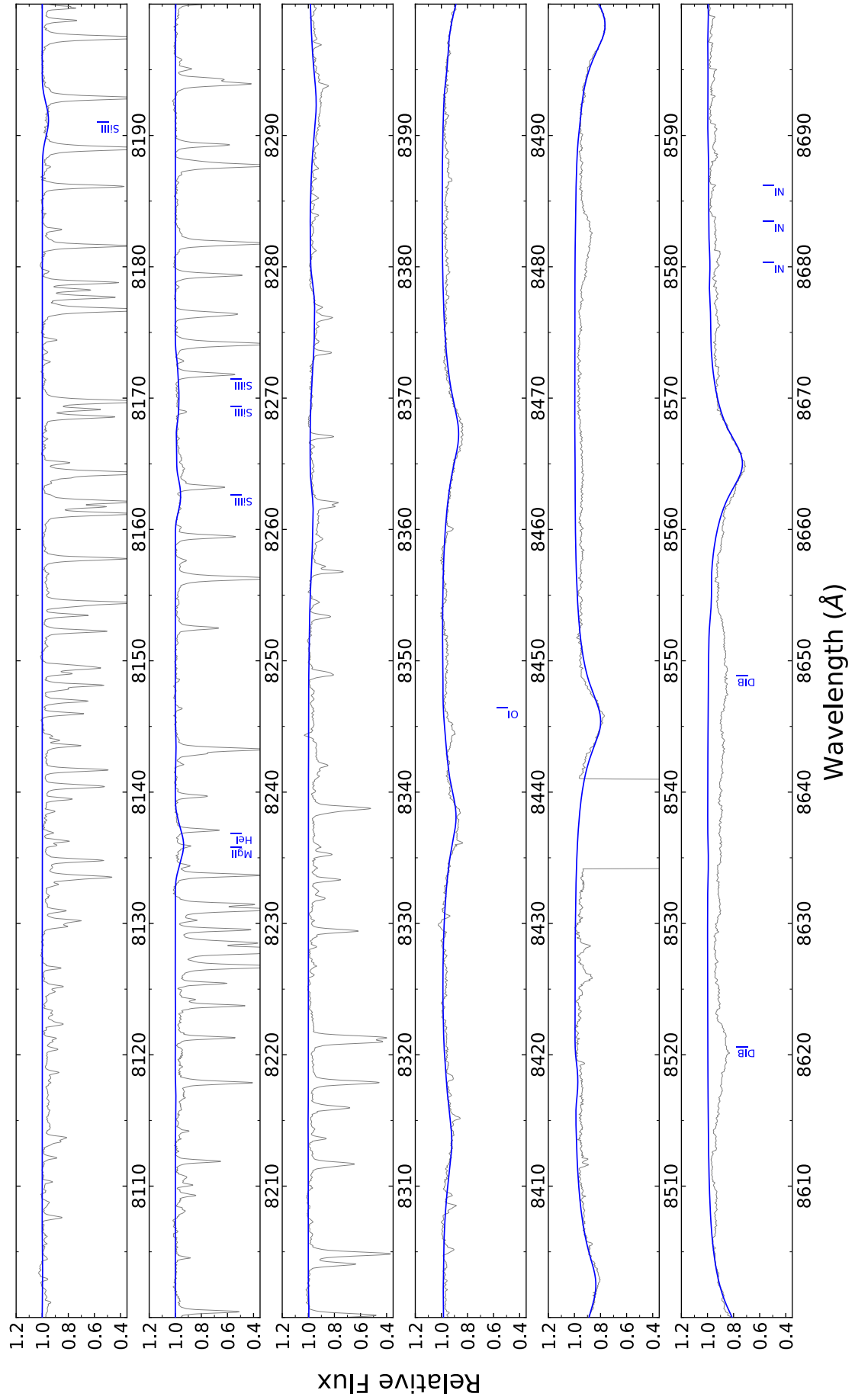


Fig. C.8. Same as Fig. C.1, but in the wavelength range $\lambda\lambda 8100\text{--}8700 \text{ \AA}$.

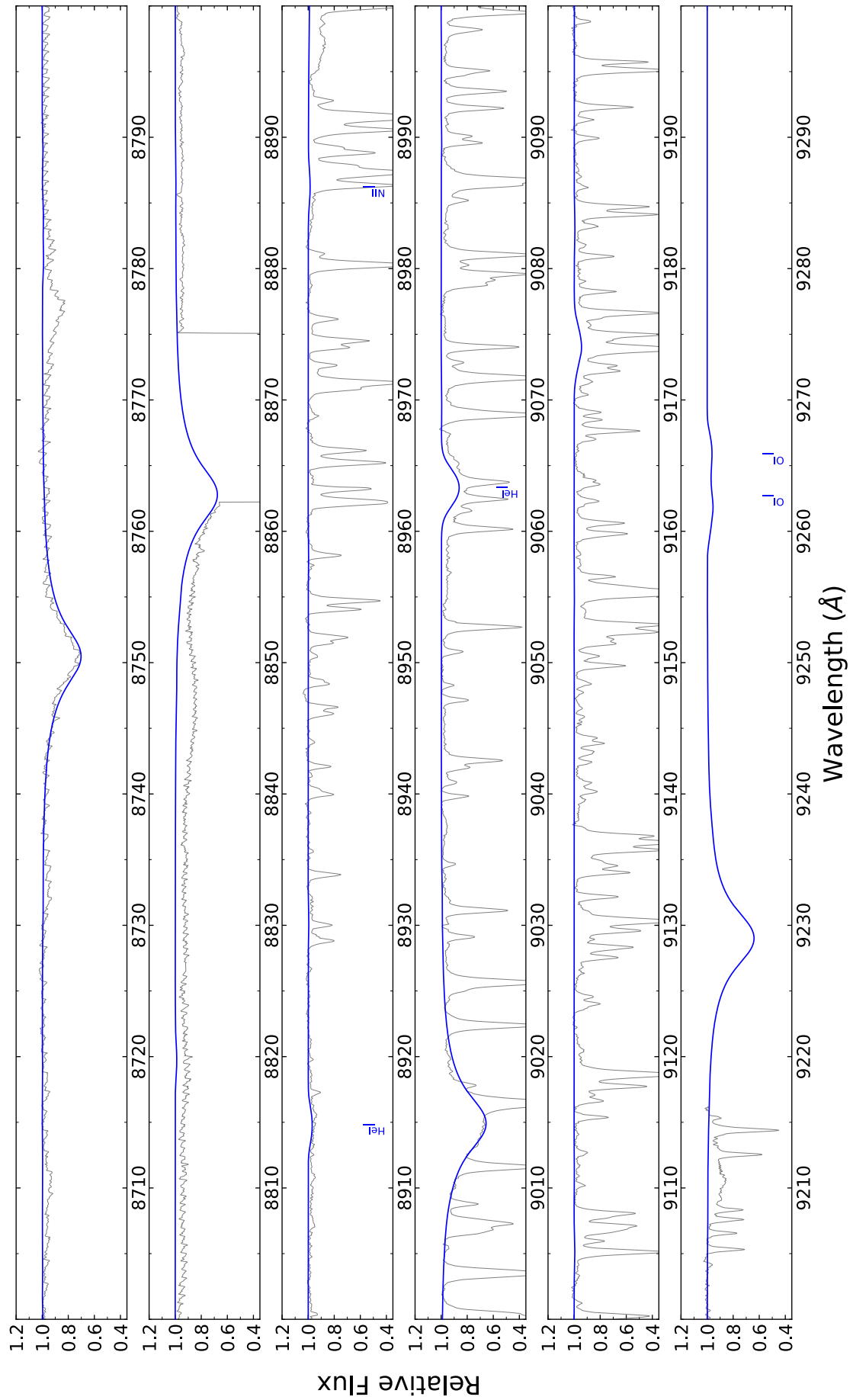


Fig. C.9. Same as Fig. C.1, but in the wavelength range $\lambda\lambda 8700\text{--}9300 \text{ \AA}$.